

West African monsoon system's responses to global ocean-regional atmosphere coupling

Article

Accepted Version

Tamoffo, A. T., Weber, T., Cabos, W., Monerie, P.-A. ORCID: <https://orcid.org/0000-0002-5304-9559>, Cook, K. H., Sein, D. V., Dosio, A., Klutse, N. A. B., Akintomide, A. A. and Jacob, D. (2024) West African monsoon system's responses to global ocean-regional atmosphere coupling. *Journal of Climate*. ISSN 1520-0442 doi: <https://doi.org/10.1175/JCLI-D-23-0749.1> Available at <https://centaur.reading.ac.uk/116590/>

It is advisable to refer to the publisher's version if you intend to cite from the work. See [Guidance on citing](#).

To link to this article DOI: <http://dx.doi.org/10.1175/JCLI-D-23-0749.1>

Publisher: American Meteorological Society

All outputs in CentAUR are protected by Intellectual Property Rights law, including copyright law. Copyright and IPR is retained by the creators or other copyright holders. Terms and conditions for use of this material are defined in the [End User Agreement](#).

www.reading.ac.uk/centaur

CentAUR

Central Archive at the University of Reading

Reading's research outputs online

Journal of Climate

West African Monsoon System's Responses to Global Ocean-Regional Atmosphere Coupling --Manuscript Draft--

Manuscript Number:	JCLI-D-23-0749
Full Title:	West African Monsoon System's Responses to Global Ocean-Regional Atmosphere Coupling
Article Type:	Article
Corresponding Author:	Alain T. Tamoffo, Ph.D Climate Service Center Germany (GERICS), Helmholtz-Zentrum Hereon, Hamburg, Germany Hamburg, GERMANY
Corresponding Author's Institution:	Climate Service Center Germany (GERICS), Helmholtz-Zentrum Hereon, Hamburg, Germany
First Author:	Alain T. Tamoffo, Ph.D
Order of Authors:	Alain T. Tamoffo, Ph.D Torsten Weber William Cabos Paul-Arthur Monerie Kerry H. Cook Dmitry V. Sein Alessandro Dosio Nana A. B. Klutse Akintomide A. Akinsanola Daniela Jacob
Abstract:	<p>This study explores the added value (AV) of a regional earth system model (ESM) compared to an atmosphere-only regional climate model (RCM) in simulating West African Monsoon (WAM) rainfall. The primary goals are to foster discussions on the suitability of coupled RCMs for WAM projections and deepen our understanding of ocean-atmosphere coupling's influence on the WAM system. The study employs results from dynamical downscaling of the ERA-Interim reanalysis and Max Planck Institute ESM (MPI-ESM-LR) by two RCMs, REMO (atmosphere-only) and ROM (REMO coupled with Max Planck Institute Ocean Model; MPIOM), at ~25-km horizontal resolution. Results show that in regions distant from coupling domain boundaries such as West Africa (WA), constraint conditions from ERA-Interim are more beneficial than coupling effects. REMO, reliant on oceanic sea surface temperatures (SSTs) from observations and influenced by ERA-Interim, is biased under coupling conditions, although coupling offers potential advantages in representing heat and mass fluxes. Contrastingly, as intended, coupling improves SSTs-monsoon fluxes' relationships under ESM-forced conditions. In this latter case, coupling features a dipole-like spatial structure of AV, improving precipitation over the Guinean coast but degrading precipitation over half of the Sahel. Our extensive examination of physical processes and mechanisms underpinning the WAM system supports the plausibility of AV. Additionally, we found that the monsoonal dynamics over the ocean respond to convective activity, with the Sahara-Sahel surface temperature gradient serving as the maintenance mechanism. While further efforts are needed to enhance the coupled RCM, we advocate for its use in the context of WAM rainfall forecasts and projections.</p>

West African Monsoon System's Responses to Global Ocean-Regional Atmosphere Coupling

Alain T. Tamoffo*¹ · Torsten Weber¹ · William Cabos² · Paul-Arthur Monerie³ · Kerry H. Cook⁴ · Dmitry V. Sein^{5,6} · Alessandro Dosio⁷ · Nana A. B. Klutse^{8,9} · Akintomide A. Akinsanola^{10,11} · Daniela Jacob¹

¹Climate Service Center Germany (GERICS), Helmholtz-Zentrum Hereon, Hamburg, Germany

²Departamento de Física Y Matemáticas, Universidad de Alcalá, Alcalá de Henares, Madrid, Spain

³National Centre for Atmospheric Science, Reading, UK

⁴Department of Geological Sciences, Jackson School of Geosciences, The University of Texas at Austin, Austin, USA

⁵Alfred Wegener Institute for Polar and Marine Research, Bremerhaven, Germany

⁶Shirshov Institute of Oceanology, Russian Academy of Science, Moscow, Russia

⁷European Commission, Joint Research Centre (JRC), Ispra, Italy

⁸African Institute for Mathematical Sciences (AIMS), Kigali, Rwanda

⁹Department of Physics, University of Ghana, Accra, Ghana

¹⁰Department of Earth and Environmental Sciences, University of Illinois Chicago, Chicago, IL, USA

¹¹Environmental Science Division, Argonne National Laboratory, Lemont, Illinois, USA

Corresponding author: Alain T. Tamoffo

Email: Alain.Tamoffo@hereon.de

Alain T. Tamoffo's ORCID: 0000-0001-8482-8881

Torsten Weber's ORCID: 0000-0002-8133-8622

William Cabos' ORCID: 0000-0003-3638-6438

Paul-Arthur Monerie's ORCID: 0000-0002-5304-9559

Kerry H. Cook's ORCID: 0000-0001-9270-4395

Dmitry V. Sein's ORCID: 0000-0002-1190-3622

Alessandro Dosio's ORCID: 0000-0002-6365-9473

Nana A.B. Klutse's ORCID: 0000-0001-5156-2765

Akintomide A. Akinsanola's ORCID: 0000-0002-0192-0082

Daniela Jacob's ORCID: 0000-0002-5249-4044

36

37 **ABSTRACT**

38 This study explores the added value (AV) of a regional earth system model (ESM)
39 compared to an atmosphere-only regional climate model (RCM) in simulating West African
40 Monsoon (WAM) rainfall. The primary goals are to foster discussions on the suitability of
41 coupled RCMs for WAM projections and deepen our understanding of ocean-atmosphere
42 coupling's influence on the WAM system. The study employs results from dynamical
43 downscaling of the ERA-Interim reanalysis and Max Plank Institute ESM (MPI-ESM-LR) by two
44 RCMs, REMO (atmosphere-only) and ROM (REMO coupled with Max Planck Institute Ocean
45 Model; MPIOM), at $\sim 25\text{-km}$ horizontal resolution. Results show that in regions distant from
46 coupling domain boundaries such as West Africa (WA), constraint conditions from ERA-
47 Interim are more beneficial than coupling effects. REMO, reliant on oceanic sea surface
48 temperatures (SSTs) from observations and influenced by ERA-Interim, is biased under
49 coupling conditions, although coupling offers potential advantages in representing heat and
50 mass fluxes. Contrastingly, as intended, coupling improves SSTs-monsoon fluxes' relationships
51 under ESM-forced conditions. In this latter case, coupling features a dipole-like spatial
52 structure of AV, improving precipitation over the Guinean coast but degrading precipitation
53 over half of the Sahel. Our extensive examination of physical processes and mechanisms
54 underpinning the WAM system supports the plausibility of AV. Additionally, we found that the
55 monsoonal dynamics over the ocean respond to convective activity, with the Sahara-Sahel
56 surface temperature gradient serving as the maintenance mechanism. While further efforts
57 are needed to enhance the coupled RCM, we advocate for its use in the context of WAM
58 rainfall forecasts and projections.

59 **KEYWORDS:** West Africa; West African monsoon system; atmosphere-only RCM; ocean-
60 atmosphere coupling; added value; precipitation

61 **1 Introduction**

62 There is a growing need to find solutions to improve weather forecasts and climate
63 projections to accurately design society's responses to climate change-related hazards (IPCC's
64 AR6 Ch10; Doblas-Reyes et al., 2021). This statement is more relevant in a context where, for
65 instance, the high variability of West African monsoon (WAM) rainfall and extreme events

66 have strong societal impacts. Despite this, significant biases still exist in the WAM system
67 simulations (e.g. Boone et al., 2010; Diallo et al. 2014). The dynamical downscaling approach
68 is undeniably part of the solution to improving the numerical representation of the African
69 climate system. It excels in providing superior resolution of orography over land, air-sea
70 interactions, land processes (e.g., albedo, land cover, sharp gradients in temperature, soil
71 moisture), potential vorticity, influence of lakes, weather fronts, which aspects are not
72 resolved by global models (Jacob and Podzun, 1997; Feser, 2006; Paeth and Mannig, 2012). It,
73 indeed, proved its effectiveness in recent decades by providing substantial added value in
74 simulating the African climate system (e.g., Dosio et al., 2015; Paxian et al., 2016; Gibba et al.,
75 2018; Wu et al., 2020). However, significant biases, both those stemming from the Regional
76 Climate Model (RCM) and inherited from boundary conditions, along with inconsistencies
77 (lack of shared internal physics and configurations) between the driving earth system models
78 (ESMs) and RCMs used for the downscaling, have the potential to lead to spurious results in
79 the dynamical downscaling (Laprise et al. 2013; Panitz et al. 2014; Saini et al. 2015). Especially
80 over West Africa (WA), a prominent hotspot for climate change on the continent (Martin and
81 Thorncroft, 2013), where the range in projected changes rivals the extent of biases in RCMs
82 (Bichet et al., 2020; Monerie et al. 2020; Zhou et al., 2020). This poses a critical concern with
83 regard to the reliability of forecasts and projections, especially in a region where the monsoon
84 system not only determines the timing but also has the potential to alter the efficiency of
85 economic activities (Niang et al. 2014). Hence, the objective of the current study is to assess
86 the efficiency of a relatively underutilized dynamical downscaling approach proposed by Sein
87 et al. (2015) in accurately simulating the WAM system. This approach involves coupling a
88 global ocean model with a stand-alone atmosphere-only RCM to enable interactive sea
89 surface temperatures (SSTs).

90 Improving the understanding of the WAM system's functioning, and subsequently,
91 improving forecasts and projections, has motivated numerous international research
92 programs and field campaign studies. For example, the African Multidisciplinary Monsoon
93 Analysis Model Intercomparison Project (AMMA-MIP; Redelsperger et al., 2006) and the
94 AMMA Land-surface Model Intercomparison Project (ALMIP; Boone et al., 2009) were
95 dedicated to this endeavor. Notable progress has been achieved in refining climate models to
96 better represent land-atmosphere coupling through initiatives such as the West African

97 Monsoon Modelling and Evaluation (WAMME; Boone et al., 2010) project. The WA region has
98 also garnered substantial research attention through various phases of the Coupled Model
99 Intercomparison Projects (CMIPs; Meehl et al., 2007; Taylor et al., 2012; Eyring et al., 2016)
100 and the COordinated Regional Climate Downscaling EXperiment project (CORDEX; Gutowski
101 et al., 2016). These concerted efforts have significantly contributed to addressing
102 uncertainties in the historical and projected climatology of WAM precipitation (e.g. Druyan et
103 al., 2009; Diallo et al., 2016; Akinsanola et al., 2017; Akinsanola and Zhou 2019; Dosio et al.,
104 2020; Tamoffo et al., 2022, 2023). However, studies conducted within the aforementioned
105 programs showed that much work still needs to be done to reduce biases, which is crucial for
106 enhancing confidence in future projections (e.g. Paeth et al., 2005; Boone et al., 2009,2010;
107 Hourdin et al., 2010; Xue et al., 2010).

108 While dynamical downscaling based on stand-alone atmosphere-only RCMs is
109 considerably suitable in better capturing smaller-scale physiographic processes and
110 mesoscale convective systems, it is not sufficient to address the biases present in ESMs. This
111 may suggest that the downscaling approach reliant on imposing SSTs onto RCMs may not be
112 the optimal method, and exploring better alternatives could be more beneficial. Previous
113 studies (e.g., Sein et al., 2014,2015; Zou and Zhou, 2016; Samanta et al., 2018) have indicated
114 that models with interactive computational SSTs at high horizontal resolution are better
115 suited for simulating climate systems characterized by strong ocean-atmosphere interactions.
116 This perspective gains more relevance in the context of monsoon systems, which typically
117 respond to changes in land-sea thermal/pressure contrasts. Modelling of monsoon systems
118 using such coupled ocean-atmosphere RCMs has prompted numerous investigations. For
119 instance, Zou and Zhou (2016) demonstrated that the regional ocean-atmosphere coupled
120 model FROALS accurately represents the East Asia monsoon system, particularly due to a
121 reduction in SST biases. Similarly, in Central India, an ocean-mixed layer model coupled with
122 an RCM significantly alleviated the dry bias observed in the atmospheric component's
123 simulation. This improvement was attributed to enhanced simulations of horizontal and
124 vertical shears, which responded to improvements in the coastal SST front over the Bay of
125 Bengal (Samanta et al., 2018). Over southern Africa, a comparison between coupled and
126 uncoupled RCMs revealed that air-sea feedback is relevant for modelling precipitation during
127 the rainfall maximum, largely due to the strong involvement of tropical processes (e.g. SST

128 variability, moisture transport, Walker- and Hadley-like circulations); however, this is not the
129 case during the onset phases of precipitation (Ratnam et al., 2015).

130 A preliminary investigation conducted by Paxian et al. (2016) highlighted, among other
131 hypotheses, that employing dynamical downscaling with an RCM coupled to a global ocean
132 model can improve the representation of WAM rainfall. The authors showed that such
133 coupling diminishes the Atlantic SST bias, resulting in a more accurate representation of air-
134 sea interactions. The reduction in SST bias triggers improvements in ocean currents,
135 particularly the coastal upwelling of the Benguela and warm Angola currents. Consequently,
136 the resulting atmospheric circulation is enhanced, leading to improvements in precipitation
137 over the tropical Atlantic, Guinea Gulf, Guinea Coast, and Central Sahel.

138 The objective of our present study builds upon the aforementioned perspectives while
139 seeking a deeper understanding of how the ocean-atmosphere coupling modulates the
140 monsoon system, both at the mesoscale and local scale. We aim to highlight a chain of
141 underlying processes that differentiate between coupled and uncoupled RCMs in the WAM
142 rainfall climatology. Unlike previous studies that utilized a similar approach, primarily focusing
143 on the SSTs (e.g., Paxian et al. 2016), our study provides the first assessment of the impacts
144 of coupling a global ocean model to an atmospheric RCM on the simulation of WAM rainfall
145 and the underlying local and regional forcing factors. This novel approach allows us, firstly, to
146 assess the potential added value provided by the ocean-atmosphere coupled approach in
147 comparison to the uncoupled approach. This assessment will stimulate discussions on the
148 appropriateness of adopting coupled RCMs instead of atmosphere-only RCMs for projection
149 purposes within the WAM system. Secondly, this approach will enable us to gain deeper
150 insights into how SSTs drive the monsoon convective system, if at all, and how the monsoon
151 convective system triggers oceanic responses (Birch et al. 2014).

152 The remainder of the document is structured as follows: in section 2, experimental,
153 observational and reanalysis data and the methods used in this study are introduced. Section
154 3 examines the differences between coupled vs. uncoupled RCMs of rainfall climatology and
155 associated added value. In section 4, processes driving the differences described in Sect. 3 are
156 investigated and the plausibility of added value derived from the coupling is highlighted.
157 Section 5 provides a discussion and concludes the paper.

158 **2. Data and methods**

159 **2.1 Data**

160 Model data utilized in this study are from a dynamical downscaling of the European
 161 Centre for Medium-Range Weather Forecasts (ECMWF) ERA-Interim reanalysis data (Dee et
 162 al., 2011), and the low-resolution ESM of the Max Planck Institute (MPI-ESM-LR; Stevens et al.
 163 2013). ERA-Interim and MPI-ESM-LR provide lateral boundary conditions for the evaluation
 164 and historical simulations, respectively. Further details on the two driving datasets and the
 165 names of the simulations stemming from each are presented in Table 1.

166 **Table 1: Details of forcing data and names of RCM experiments used in this study.**

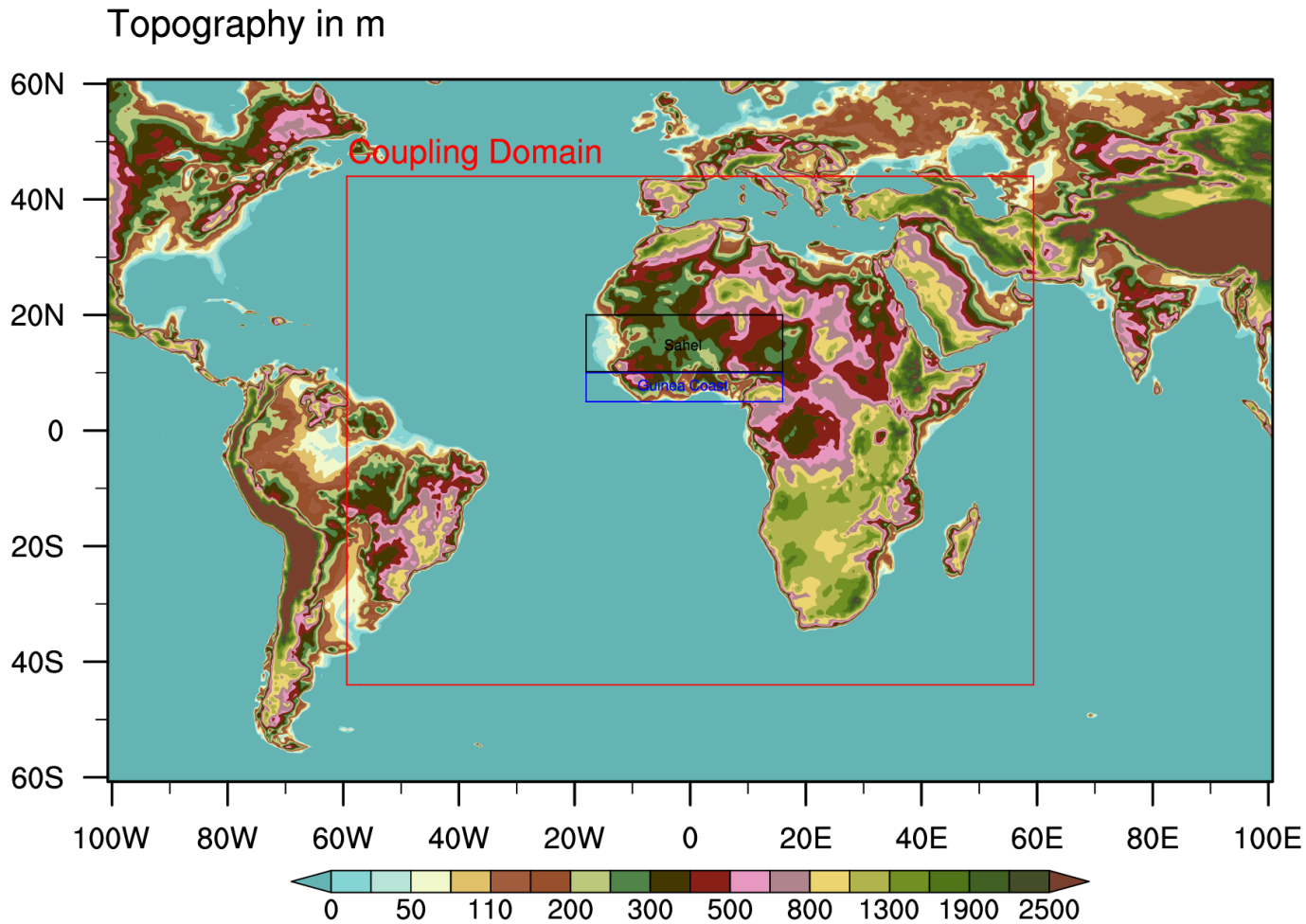
Institution	ESMs' names	RCMs (0.22° x 0.22°)	Experiment names	Ocean-atmosphere	Periods used	Reference
European Centre for Medium Range Weather Forecasts	ERA-INT (0.75° x 0.75°)	REMO ROM	REMO-ERA ROM-ERA	Uncoupled Coupled	1980-2005	Dee et al. (2011)
Max Planck Institute for meteorology	MPI-ESM-LR (1.9° x 1.9°)	REMO ROM	REMO-MPI-ESM-LR ROM-MPI-ESM-LR	Uncoupled Coupled	1980-2005	Stevens et al., (2013)

167

168 Two distinct regional climate models are used as the dynamical downscaling tools in
 169 this study. The first is the regional climate model REMO (Jacob 2001). REMO is an atmosphere-
 170 only RCM developed at the Max Planck Institute for Meteorology in Hamburg, Germany, and
 171 its maintenance is currently performed at the Climate Service Center Germany (GERICS). The
 172 second is the regionally-coupled model ROM (Sein et al. 2015; Cabos et al. 2020), which is a
 173 combination of REMO as the atmospheric component and Max Planck Institute Ocean Model
 174 (MPIOM; Jungclaus et al. 2013) as the ocean component. Refer to Sein et al. (2015), Cabos et
 175 al. (2020) and Weber et al. (2022) for full details about the physical configurations of the global
 176 ocean-regional atmosphere coupled RCM ROM used in the present study. Briefly, the ocean
 177 model underwent a two-cycle spin-up, forced by the 1958-2002 ERA-Interim data, totaling 90
 178 years. At the start of the spin-up, the ocean is at rest, with its temperature and salinity derived
 179 from the Levitus January climatology. Over these 90 years, the ocean velocities, salinity, and
 180 temperature for MPIOM are adjusted, reaching a state of quasi-equilibrium, especially in the
 181 upper ocean layers. The subsequent spin-up of the coupled models ROM-ERA and ROM-MPI

182 continued from the final state of the forced MPIOM run. The REMO-MPI setup underwent
183 further spin-up using the MPI-ESM-LR forcing data from 1950. Meanwhile, ROM-ERA was
184 forced by reanalysis data from ERA40 (1958-1980) and ERA-Interim (1981-2002). During the
185 coupled spin-up, consideration was given to the prolonged thermohaline and dynamical
186 adjustments, particularly in deeper layers. During the coupled spin-up, special attention was
187 paid to prolonged thermohaline and dynamical adjustments, particularly in deeper layers. For
188 this reason, ROM-ERA underwent spin-up first with ERA-Interim and then with ERA40, as the
189 warming trend observed during the 1981-2002 run rendered it unsuitable as the initial state
190 for the production run. Instead, the ROM-ERA production run commenced from a state closer
191 to observed conditions. The impact of forcing changes was deemed insignificant after one or
192 two years, particularly in SSTs, therefore, the production run for the two setups commenced
193 when the initial state approximated a quasi-equilibrium (with a realistic initial state for ROM-
194 ERA), despite limitations in discarding initial years. As demonstrated by Paxian et al. (2016) in
195 the context of decadal predictions, and by Sein et al. (2015) and Cabos et al. (2017) for
196 historical simulations, the Atlantic SST bias is significantly reduced in coupled regional
197 simulations. This reduction is attributed to the representation of fine-scale air-sea interactions
198 at high atmosphere and ocean resolutions, which improve deficient GCM winds and surface
199 ocean currents, intensify the cold water upwelling of the Benguela current, and decrease the
200 southward expansion of the warm Angola current. Consequently, the simulated ITCZ remains
201 in its observed position over the northern Guinea Coast.

202 Both REMO and ROM experiments were carried out over a domain slightly larger than
203 the usual CORDEX-Africa domain (see Fig. 1).



204

205 Fig. 1 The coupling area (red box) is displayed along with the topography of the domain (in meters) from
 206 NASA GTOPO30. Also shown are the Guinea Coast (blue box) and Sahel (black box), the combination of
 207 which forms the West Africa region.

208

209 The evaluation simulations, i.e., the dynamical downscaling forced by ERA-Interim,
 210 span the period from 1980 to 2014, whereas the historical runs, i.e., forced using MPI-ESM-
 211 LR as a lateral boundary condition, cover the period 1950-2005. The ERA-Interim-forced
 212 simulation aids in understanding the models' behavior under conditions close to reality.
 213 Conversely, the selection of MPI-ESM-LR for the historical simulation is driven by the need to
 214 avoid biases due to inconsistencies. Indeed, both MPI-ESM-LR and ROM share the same ocean
 215 component, and both REMO and ROM utilize identical physical parameterizations and a
 216 dynamical core, as ECHAM (the atmospheric component of MPI-ESM-LR; Jacob et al., 2012).
 217 This minimizes inconsistencies between the forcing and downscaling models. Simulations
 218 were done at $0.22^\circ \times 0.22^\circ$, i.e., $\sim 25\text{-km}$ horizontal resolution, and the timeframe used for
 219 analyses is 1980-2005, based on the availability of reference datasets. However, the

220 configuration of the oceanic component MPIOM is slightly different. As Cabos et al. (2020)
 221 described, it consists of a horizontal resolution reaching 10 km (eddy-permitting) in the
 222 vicinity of the Iberian Peninsula. It gradually reduces up to 100 km in the southern seas.
 223 Hereafter, the terms REMO-ERA and REMO-MPI (ROM-ERA and ROM-MPI) will be used when
 224 referring to the uncoupled (coupled) simulations.

225 The experimental datasets are compared against three gauge-based, satellite-derived
 226 or combined datasets, along with two gridded atmospheric reanalysis products (see Table 2
 227 for full details). Notably, assessing climate models over equatorial Africa is very challenging
 228 because of the scarcity of ground-based measurements (Nicholson et al. 2019). The utilization
 229 of multiple reference datasets is the most often used solution to account for observational
 230 uncertainties. Given that reanalysis products are obtained from the assimilation of scattered
 231 ground-based measurements, we do not expect them to reproduce the exact observed
 232 climate, especially for precipitation, as also demonstrated by Gbode et al. (2023) for WA.
 233 However, because winds, specific humidity, and geopotential heights are constrained by
 234 observations, the water cycle produced is more accurate than from climate models. From this
 235 perspective, reanalysis data are used in this study qualitatively rather than quantitatively (i.e.,
 236 as guidance). In other words, the reanalysis will enable us to ensure that the simulations
 237 realistically represent the baseline structure of the WAM system.

238 **Table 2: Description of reanalysis and satellite/gauge datasets employed for the inter-comparison**
 239 **analysis.**

Dataset	Institution	Horizontal Resolution	Periods used	Reference
CRU-TS4.05	Center for Atmospheric Research (NCAR) Climate Research Unit, University of East Anglia	0.5° x 0.5°	1980-2005	Harris et al., (2020)
GPCC-v2020	Global Precipitation Climatology Centre	0.25° x 0.25°	1980-2005	Schneider et al., (2022)
CHIRPS2	Climate Hazards InfraRed Precipitation with Stations	0.05° x 0.05°	1981-2005	Funk et al., (2015)
ERA5	European Centre for Medium-Range Weather Forecasts	0.25° x 0.25°	1980-2005	Hersbach et al., (2020)
MERRA2	The Modern-Era Retrospective analysis for Research and Application, version 2	0.5° x 0.66°	1980-2005	NASA (2016)

240

241 2.2 Methods

242 The study area is WA (18°W-16°E; 5°-20°N), which consists of two main regions: the
243 humid Guinea Coast (18°W-16°E, 5°-10°N; indicated by the blue box in Fig. 1) and the
244 transitional Sahel climate region (18°W-16°E, 10°-20°N; indicated by the black box in Fig. 1).
245 The Guinea Coast experiences two rainfall maxima in June and September, and a drier period
246 in August (as known as “the little dry season”) during which monthly rainfall weakens (<3 mm
247 d⁻¹). In the Sahel region, the rainfall regime is unimodal, with precipitation peaking in August
248 (>6 mm d⁻¹). As a result, we therefore focus our analyses on the July-August-September (JAS)
249 season. This period corresponds to the peak of the WAM rainfall, as highlighted by Nicholson
250 (2013), and corresponds to the maturation of physical processes and mechanisms that drive
251 the WAM rainfall.

252 We assess how REMO and ROM improve the simulation of climatological WAM rainfall
253 using the added value (AV) statistical metric, as defined by Dosio et al. (2015) and quantified
254 using the following the equation:

$$255 \quad AV = \frac{(X_{REMO} - X_{ref})^2 - (X_{ROM} - X_{ref})^2}{\text{Max}((X_{REMO} - X_{ref})^2, (X_{ROM} - X_{ref})^2)} \quad (1)$$

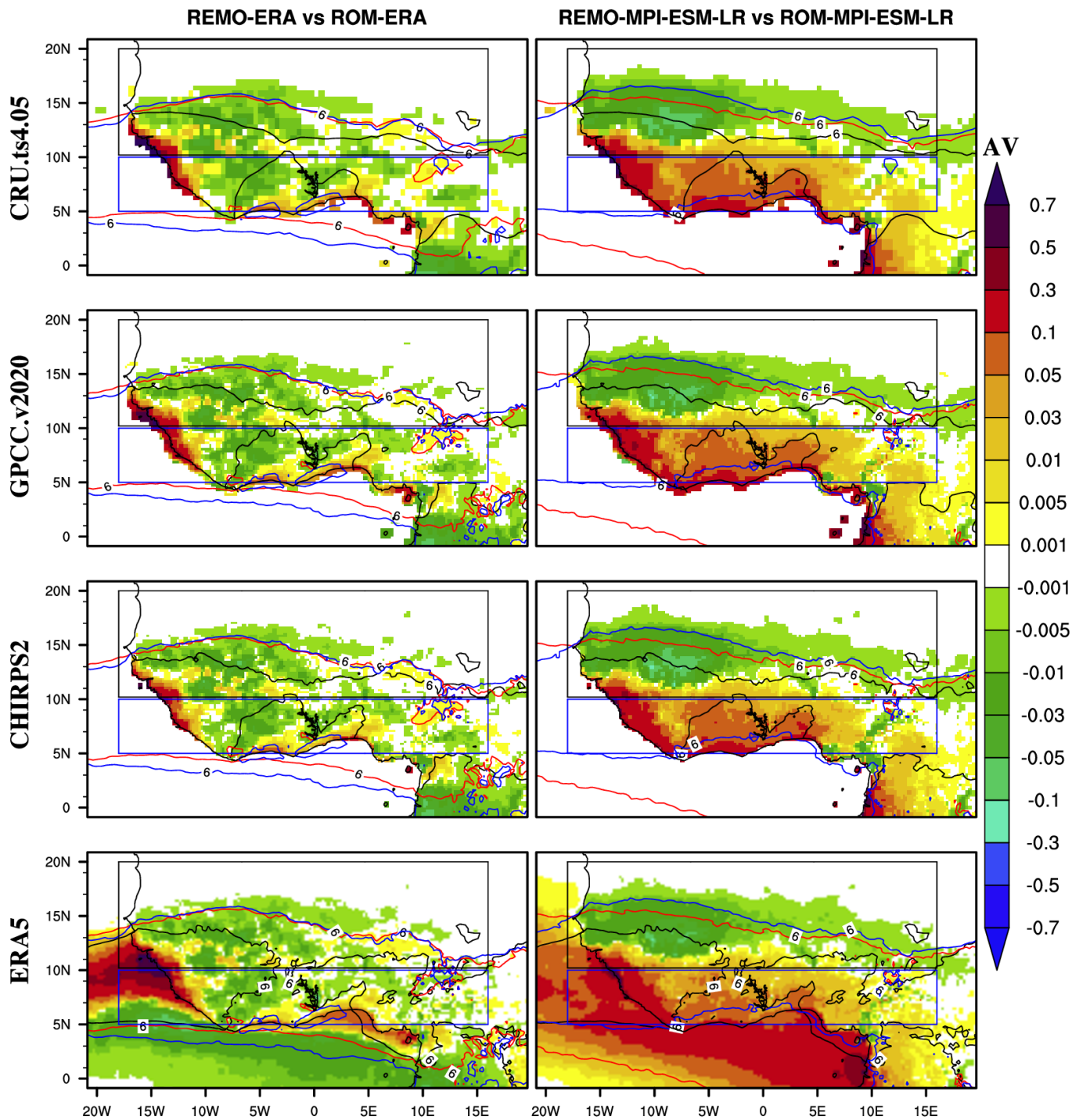
256 where X represents the climatological spatial distribution of precipitation for the considered
257 experiment (X_{REMO} or X_{ROM}) or reference dataset (X_{ref}). Following Dosio et al. (2015), the
258 values of the AV are normalized by their maximum (Max) so that $-1 \leq AV \leq 1$. AV directly
259 compares REMO and ROM such that a positive AV indicates that the ROM coupled simulation
260 improves over the REMO uncoupled simulation. Conversely, a negative AV indicates that the
261 coupling does not lead to an improvement in the representation of the climate system. We
262 have arbitrarily selected the threshold of 10^{-3} , i.e., the nearest thousandth ($-10^{-3} < AV < +10^{-3}$),
263 to highlight areas where the coupled model ROM exhibits equal performance to the
264 uncoupled model REMO. The mean precipitation bias and the precipitation bias’ statistical
265 significance at 95% level through the two-tailed Student t-test is assessed. This helps to
266 understand whether the improvement or deterioration is associated with an overestimation
267 or underestimation of simulated rainfall.

268 To understand the reasons behind the sign of AV for each model group, we examined
269 and compared REMO and ROM results in terms of their ability to reproduce the fundamental

270 processes underlying the WAM system. One key distinction between the atmosphere-only
271 and coupled ocean-atmosphere climate models is that the former respond to prescribed SSTs
272 from the forcing ESMs, while the latter benefit from the more physical representation of heat
273 and mass fluxes provided by interactive SSTs. Models with prescribed SSTs are not
274 energetically closed at the surface, while coupled models are. Therefore, we examined how
275 both groups of simulations represent regional features associated with the WAM, specifically,
276 the marine Inter-Tropical Convergence Zone (ITCZ) and continental monsoon rain-band
277 (d'Orgeval, 2008), the mean seasonal positioning of the Sahara heat low (SHL; Lavaysse et al.
278 2009,2010), the dynamics and intensity of the monsoon flows triggered by the land-sea
279 thermal and pressure contrasts and which drive land-sea interactions (Fontaine et al. 1999;
280 Parker et al. 2005); the West African westerly jet (WAWJ; Pu and Cook 2010,2012), the mid-
281 tropospheric African Easterly Jet (AEJ; Cook 1999; Nicholson and Grist 2003; Thorncroft et al.
282 2003), the upper-tropospheric Tropical Easterly Jet (TEJ; Nicholson and Klotter 2020) and the
283 atmospheric instability/stability associated with the convection (Fontaine et al. 1999). Done
284 this way, an experiment brings plausible AV when the improvement occurs for the right
285 reasons, meaning if the positive AV values are effectively accompanied by an improved
286 representation of the underlying drivers that underpin the monsoon system (Tamoffo et al.
287 2020).

288 **3. REMO vs ROM: the added value (AV)**

289 The performance-based assessment of ROM against REMO in adding value to the
290 mean JAS rainfall climatology is shown in Figure 2. The reliability of these findings relies on
291 the consistency observed across multiple reference datasets, including CRU.ts4.05,
292 GPCC.v2020 and CHIRPS2 observations, and the ERA5 reanalysis.



293
 294
 295
 296
 297
 298
 299
 300
 301

Fig. 2 Added value (AV) of mean JAS WA precipitation in ROM compared to REMO experiments. The reference datasets used are the observations CRU.ts.05, GPCC-v2020 and CHIRPS2, and the reanalysis ERA5, over the period 1980 to 2005, except CHIRPS2 that covers the period 1981-2005. Positive (negative) values indicate a lower (higher) precipitation bias of ROM compared to REMO. Contours indicate the position of the rain-band (i.e., precipitation larger than 6 mm/day) from the reference dataset (black), REMO (red) and ROM (blue). The blue box denotes the **Guinea Coast** (5°-10°N: 18°W-16°E) while the black box denotes the **Sahel** (10°-20°N: 18°W-16°E).

302 The choice of ERA5 is firstly motivated by its ability to reliably mimic the WAM rainfall
303 seasonality, with the variability within the range of observational uncertainties (Quagraine et
304 al. 2020; Gbode et al. 2023). Secondly, ERA5 features high horizontal and vertical resolutions
305 among reanalyses available over equatorial Africa, crucial for capturing synoptic-scale
306 mechanisms. Additionally, ERA5 is produced at an hourly time scale, essential for accounting
307 for transient processes (Hersbach et al. 2020). We omitted MERRA2 ($0.5^\circ \times 0.66^\circ$) from this
308 analysis to prevent misinterpretation arising from interpolation errors. Notably, the alignment
309 of results from ERA5 with those of three observations is of significance (Figure 2). This
310 consistency is particularly crucial as ERA5 will be used in subsequent analyses as a reference
311 dataset to diagnose the physical mechanisms underlying the WAM system. The uncertainties
312 related to the extent of improvement, deterioration and neutrality are also indicated, using
313 the standard deviation of the percentage values obtained from the four reference datasets.

314 Under the reanalysis-forced mode, where simulations are driven by the ERA-Interim
315 reanalysis, the spatial pattern of AV includes a degradation ($AV < -0.001$) of the simulated
316 precipitation over nearly half of the Guinea Coast (around $47.5\% \pm 2.5\%$ of the area; see Figure
317 2 and Fig. S1a) and a substantial portion of the southwestern Sahel (around $30\% \pm 1.30\%$ of
318 the Sahel; see Figure 2 left column and Fig. S1b). There are improvements ($AV > +0.001$) in a
319 small portion of the coastal areas of southwestern WA, extending towards the ocean (Figure
320 2), and over localized sparse areas (with combined percentage area reaching $33\% \pm 2\%$). The
321 results, based on the four reference datasets, are in agreement, showing improvements in
322 approximately $10\% \pm 0.94\%$ of the Sahel. However, towards the northern and in most parts of
323 the eastern Sahel (around $60\% \pm 1.63\%$ of the total area), REMO and ROM exhibit equivalent
324 performance in simulating the mean seasonal precipitation climatology ($-0.001 \leq AV \leq 0.001$).
325 Compared to the reference datasets, both the uncoupled REMO and coupled ROM models
326 simulated higher precipitation along the Guinean coast and over much of the Sahel, and REMO
327 is drier than ROM everywhere (Fig. S2). Furthermore, it is notable that the simulated
328 continental rainband appears to be too wide in both REMO and ROM simulations (Fig. 2).

329 When integrated under the ESM-forced mode, i.e., when the MPI-ESM-LR is used as
330 the lateral boundary condition, the spatial pattern of AV features a dipole-like structure,
331 consisting of positive AV (i.e., improvements) over almost all the Guinea Coast (around $88\% \pm$
332 2.52% ; Fig. 2 right column and Fig. S1a) and a small part of south-central and western Sahel

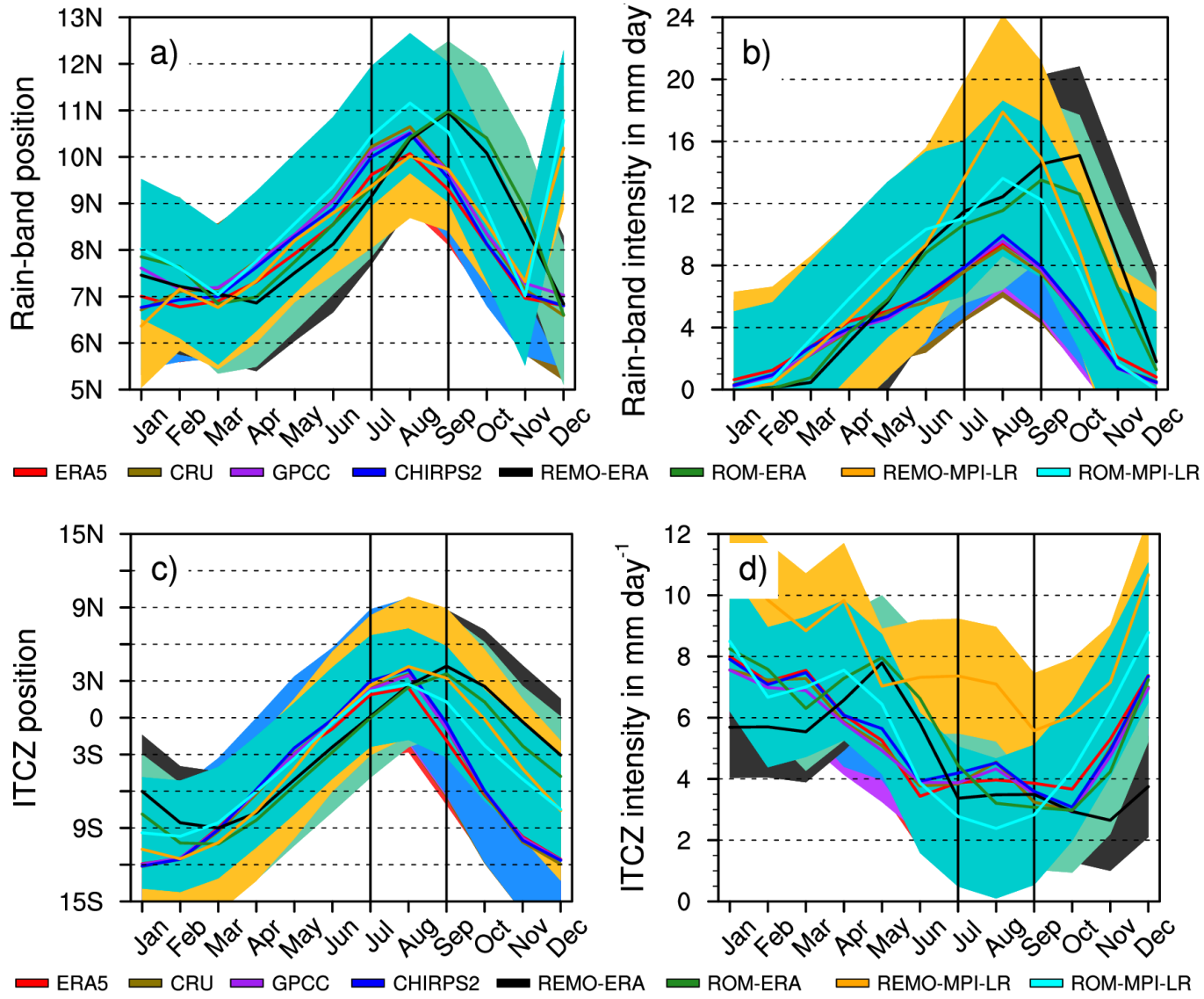
333 (approximately $10\% \pm 2.75\%$; Fig. 2 and Fig. S1b), and negative AV (degradations) over almost
 334 half of the Sahel ($46\% \pm 3\%$). Both REMO and ROM exhibit equivalent performance over 40%
 335 $\pm 3.41\%$ of the Sahel. These Models simulate higher precipitation amounts in most regions of
 336 the Guinean Coast and southern Sahel, relative to all reference datasets (Fig. S2). ROM-MPI
 337 decreases the wet bias over the Guinea coast while strengthening the wet bias over the Sahel
 338 in comparison to REMO-MPI (Fig. S2). Furthermore, ROM improves the extent to the south of
 339 the southern side of the rain-band, but there is no significant change along the northern side.

340 The descriptions above regarding how the southern and northern edges of the WAM
 341 rain-band respond to coupling have drawn our attention to how the mean locations, not only
 342 of the WAM rain-band but also of the marine ITCZ, are represented in the uncoupled and
 343 coupled experiments. The response of the marine ITCZ to coupling is also investigated because
 344 there is a link between the position and intensity of the ITCZ and precipitation in the Sahel. A
 345 shifted ITCZ further north induces more precipitation in the Sahel and vice versa, through a
 346 chain of processes described in Biasutti (2019) and references therein. Differences in the
 347 location of the ITCZ will provide information on how simulations of the large-scale drivers of
 348 the West African rainfall (e.g. Hwang et al. 2013; Song et al. 2018) are affected by the coupling.

349 To gain a general overview, we located the precipitation's barycentre, following
 350 d'Orgeval, (2008). In fact, the WAM rain-band is determined by computing the zonal mean
 351 ($18^\circ\text{W}-16^\circ\text{E}$) of the precipitation's barycentre, localised throughout latitudes $5^\circ-20^\circ\text{N}$ (Fig. 3a)
 352 using Equation 2 as follows:

$$353 \quad G(t) = \frac{\sum_{i=1}^n y_i P_i}{\sum_{i=1}^n P_i} \quad (2)$$

354 where P_i is precipitation at latitude y_i . The barycentre G is computed for each time step t . The
 355 intensity of the WAM rain-band is defined as the precipitation rate at the barycentre's location
 356 (Fig. 3b). A similar exercise is employed to obtain the mean seasonal position of the ITCZ (Fig.
 357 3c) and its intensity (Fig. 3b), but using the longitudinal band $60^\circ\text{W}-60^\circ\text{E}$ and latitudinal band
 358 $30^\circ\text{S}-30^\circ\text{N}$, following Monerie et al. (2013). For consistency, precipitation is masked over the
 359 ocean specifically when calculating the WAM rain-band positions and intensity. This was done
 360 since the three observations (CRU.ts4.05, GPCC.v2020, and CHIRPS2) lack data over the ocean.



361

362

363 **Fig. 3** The mean latitudinal location of the (a) WAM rain-band and (c) intertropical convergence zone (ITCZ),
 364 defined as the barycentre of the zonal mean 18°W-16°E and 60°W-60°E respectively, of the precipitation,
 365 localized over the latitudes 5°-20°N and 30°S-30°N respectively, following d’Orgeval (2008); the mean
 366 intensity of the (b) WAM rain-band and (d) ITCZ, defined as the rainfall amount recorded at the barycentre.
 367 The corresponding shaded area in color represents the standard deviation, indicating the variability in both
 368 the location (a-c) and intensity (b-d) of the rain-band and ITCZ, respectively. The black bars denote the
 369 July-August-September months.

370

371 The three observational datasets consistently show that the WAM rain-band is
 372 centered around 10°N in July and reaches its northernmost position at around 10.5°N in
 373 August, before starting its southward retreat in September (Fig. 3a). The reanalysis-forced
 374 runs are the least effective in positioning the WAM rain-band - they peak in September instead
 375 of in August as in the MPI-ESM-LR-forced simulations and the observations. Similarly, the rain-
 376 band intensity peaks in October in REMO-ERA and in September in ROM-ERA, instead of

377 August (Fig. 3b). The ESM-forced runs outperform reanalysis-forced runs; however, they also
378 misrepresent the latitudinal positioning of the rain-band. Indeed, the uncoupled REMO-MPI
379 experiment positions the WAM rain-band too far south with respect to CRU.ts4.05,
380 GPCC.v2020 and CHIRPS2, but in quasi-agreement with the ERA5 reanalysis. In contrast, the
381 coupled ROM-MPI experiment places the WAM rain-band too far north. Nevertheless, both
382 REMO and ROM forced by MPI-ESM-LR fall within the standard deviation of the observations
383 (Fig. 3a). Additionally, although they overestimate the intensity of the rain-band (Fig. 3b), they
384 nonetheless capture the timing of its occurrence. Notably, the coupled ROM-MPI run
385 improves the WAM rain-band intensity relative to the uncoupled REMO-MPI run. Similarly,
386 the reanalysis-forced simulations also misplace the intraseasonal locations of the ITCZ (Fig.
387 3c). They place the northernmost position in September instead of August, although its
388 position around 3°N is better represented. ESM-forced simulations manage to capture the
389 timing of the intraseasonal migration of the ITCZ, with the coupled ROM-MPI experiment
390 performing better than the uncoupled REMO-MPI experiment. In terms of intensity (Fig. 3d),
391 the uncoupled REMO-MPI simulation is the least accurate, with the three-month intensity
392 completely outside the standard deviation of the observations. Its counterpart, the coupled
393 ROM-MPI simulation improves but still underestimates the intensity of the ITCZ, with the
394 August value outside the standard deviation of the observations.

395 It is worth mentioning that ESM-driven simulations successfully replicate the spatial
396 structure of the rainfall trend, exhibiting enhanced rainfall in the major part of the Sahel and
397 reduced rainfall in most parts of the Guinea Coast (Fig. S3). This concurs with the spatial
398 pattern of added value as simulated by the coupled model ROM-MPI. A meridional
399 (north/south) dipole is associated with a northward shift of the monsoon, aligning with our
400 understanding of the variability in WAM rainfall and with the observed recovery trend
401 (Biasutti, 2019). However, the absolute amplitude of the trend is overestimated. This suggests
402 that the primary driver of the precipitation trend remains unaltered by the coupling effect.
403 Consequently, this influential factor is not, or at least not predominantly, linked to SSTs over
404 the eastern equatorial Atlantic. Moreover, trends in precipitation, such as the drying observed
405 during the 1970s-1980s followed by subsequent recovery, are also associated with external
406 forcings such as greenhouse gases and anthropogenic aerosols (Monerie et al., 2022). It is
407 worth noting that improvements in SSTs were not uniform across all oceanic basins.

408 Furthermore, the coupling was implemented regionally rather than globally, indicating that
409 outside the coupling domain (see Fig. 1), the SST is influenced by the global (biased) forcing
410 data. These observations align with previous studies that have implicated large-scale forcing
411 factors in the occurrence of the 1970s and 1980s drought in the Sahel (e.g., Janicot et al.,
412 1996).

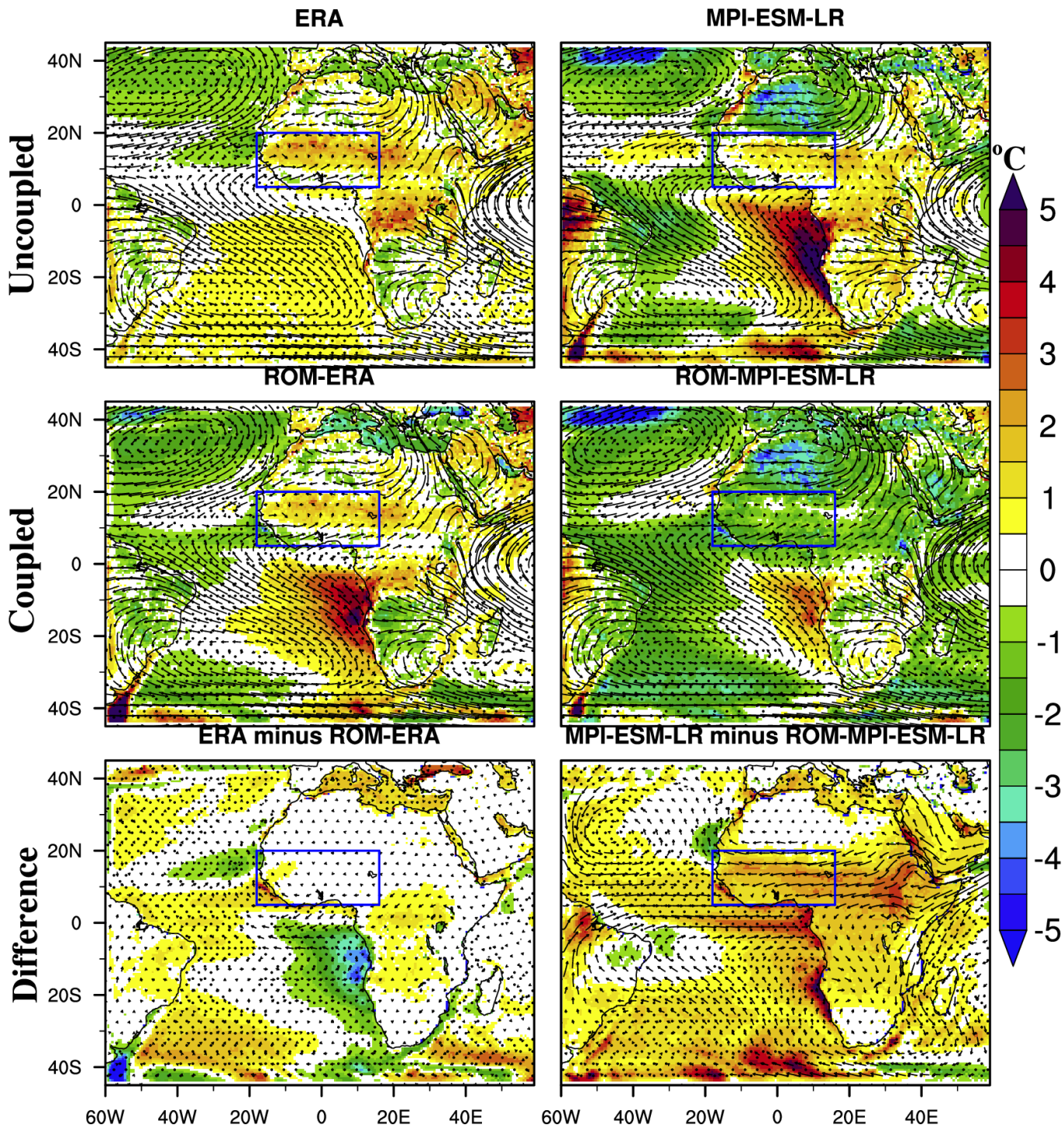
413 The coupling proves to be more beneficial under ESM-forced conditions, i.e., when
414 forced by MPI-ESM-LR, than under reanalysis-forced conditions, i.e., when driven by ERA-
415 Interim, particularly over the Guinean coast. This result is consistent with the expected finding
416 that under reanalysis-forced conditions, the coupling is not subject to the influence of biased
417 boundary conditions. Instead, the atmospheric component REMO, which inherits SSTs derived
418 from observations over the ocean, is influenced by the ERA-Interim reanalysis and not by the
419 oceanic component MPIOM. Coupling under these conditions has biased the simulated
420 atmospheric fields, although it has the potential advantage of better physically representing
421 the heat and mass fluxes due to an interactive SST. ROM deteriorates the precipitation
422 climatology in almost half of the Sahel, although it improves the positioning and intensity of
423 the ITCZ during most of the monsoon time. The enhancement in the ITCZ representation
424 suggests a better depiction of fine-scale air-sea interactions at higher atmospheric and
425 oceanic resolutions in ROM, leading to a simulated ITCZ that is not shifted southward (Paxian
426 et al. 2016). This leads to the hypothesis that the negative AV in the Sahel is associated with
427 some local or regional WAM features that are either deteriorated or not improved by ROM.
428 The next section addresses this issue.

429 **4. The reasons behind added value (AV)**

430 This section delves into the factors influencing the sign of AV. Our analysis centers on
431 two key aspects. Firstly, we explore how ROM simulates the WAM's drivers compared to
432 REMO, aiming to clarify the plausibility of the AV results. Secondly, we investigate the
433 sensitivity of the WAM's drivers to air-sea interactions. This secondary aspect enhances our
434 comprehension of the mechanisms underlying the WAM, a knowledge valuable for both
435 forecasting and projection purposes.

436 **4.1 The SST response to coupling**

437 SSTs affect atmospheric moisture content, which can be advected and result in
438 changes in precipitation over land (Cook and Vizy, 2006). In addition, SST gradients are
439 associated with moisture convergence and ITCZ location, global energy budgets, pressure
440 gradients and monsoonal circulations (Cook, 1999; Rodríguez-Fonseca et al. 2015). These
441 processes are discussed in Section 4.3. Consequently, in Figure 4, we depict the response of
442 SSTs over the eastern Atlantic Ocean to coupling by computing the SST biases, i.e., the
443 difference between the mean SST climatology of the simulations and that of ERA5 reanalysis.
444 We focus on SSTs when first describing Figure 4 because the coupling was performed over the
445 oceans. Thus, land surface temperatures respond to the coupling over oceans, aiding in the
446 understanding of surface temperature gradients subsequently analyzed in the next section.



447

448 **Fig. 4** Mean (1980-2005) JAS SST biases (shaded) computed relative to the ERA5 reanalysis, and the mean
 449 JAS circulation at 850 hPa. Also shown are the differences between the ERA and MPI-ESM-LR experiments
 450 and their corresponding ROM-downscaled experiments. For the 4 top (2 bottom) panels, the stipples occur
 451 where the difference between the dataset under consideration and the ERA5 reanalysis dataset (the
 452 difference between ERA/MPI-ESM-LR and ROM) is statistically significant at the 95% confidence level after
 453 a Student's t-test is applied. The blue boxes indicate the WA region.
 454

454

455

456

ERA (ERA-Interim reanalysis) exhibits the weakest warm SSTs bias (+0.69°C) over the entire southern Atlantic Ocean, including the South Atlantic High-pressure system. MPI-ESM-

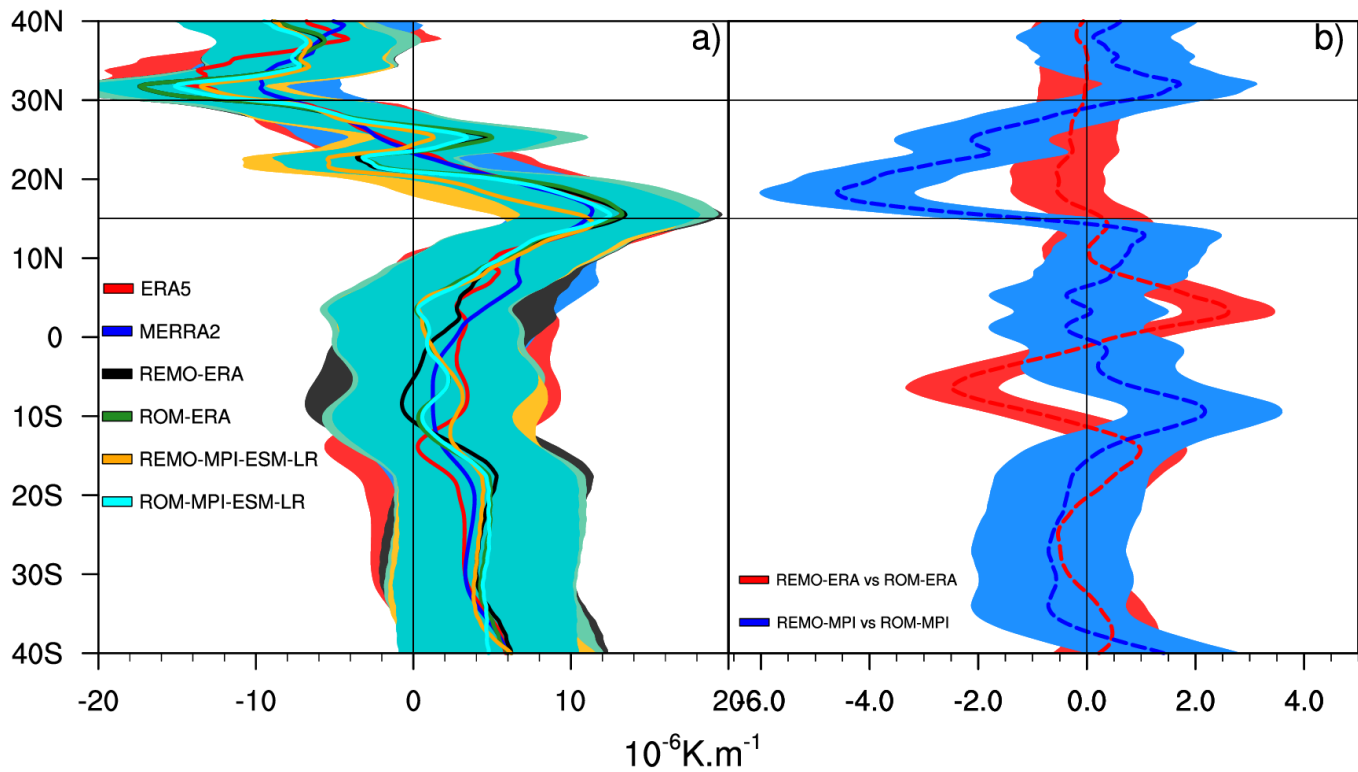
457 LR shows the highest positive SST bias (+2.19°C) over the entire Gulf of Guinea and Benguela-
458 Angola coastal seas. These positive biases cover a large area extending southward along
459 coastal areas and even over the South Atlantic High region. Figure S4 reveals that the coupling
460 degrades SSTs in the reanalysis-forced ROM-ERA run. This experiment warms SSTs (+2°C), yet
461 ERA-Interim previously exhibited a weaker SST bias value (+0.69°C). In contrast, ROM
462 improves SSTs over the eastern Atlantic Ocean compared to MPI-ESM-LR (Fig. S4). Specifically,
463 ROM-MPI reduces the magnitude of warm SST bias (+0.54°C) that previously featured MPI-
464 ESM-LR (+2.19°C). Generally, the driving MPI-ESM-LR appears warmer in most parts of the
465 Atlantic Ocean compared to ROM-MPI-ESM-LR. As a likely response, ROM-MPI-ESM-LR
466 experiences higher sea level pressure (not shown) in most regions of the ocean than REMO-
467 MPI-ESM-LR.

468 Figure S5 shows that the cooler SSTs simulated by ROM-MPI compared with REMO-
469 MPI lead to a decrease in evaporation over the eastern Atlantic Ocean. The weakening in the
470 evaporation is larger in coastal areas (north of the equator) with a change in the bias sign.
471 Inland and compared to REMO-MPI, ROM-MPI decreases evaporation over the Guinea Coast,
472 but enhances evaporation over the Sahel. The strengthening of evaporation over the Sahel
473 aligns with the previously noted bolstered precipitation (Tamoffo et al. 2023). On the other
474 hand, the increase in evaporation over the Sahel suggests the influence of coupling on the
475 radiative budget (Vizy et al., 2013), with feedback on regional WAM features such as the SHL.
476 This point is further explored in section 4.5. At first glance, changes in SSTs are associated with
477 modifications in air-sea interactions, including the land-ocean thermal contrast and the
478 resulting pressure contrast that determines the force of monsoon fluxes. This aspect is
479 examined in the following section.

480 **4.2 Air-Sea interactions' response to coupling**

481 Figure S2 has demonstrated that under the reanalysis-forced mode driven by ERA-
482 Interim reanalysis, there are no significant differences between REMO and ROM in terms of
483 precipitation magnitude across WA, with REMO only slightly drier than ROM. However, the
484 ESM-forced experiments, i.e., when driven by MPI-ESM-LR, showed that REMO is moister than
485 ROM along the Guinean coast but drier than ROM in the Sahel region. We hypothesize that
486 depending on the forcing mode, changes in air-sea interactions resulting from coupling could
487 be responsible for the spatial pattern of moistening or drying in each experiment. Surface

488 thermal and pressure gradients or contrasts act as drivers for these land-sea interactions
 489 (Zhao et al. 2005). To test our hypothesis, we diagnosed the representativeness of these
 490 factors in each simulation. Figure 5 compares REMO and ROM against the reanalysis datasets
 491 (Fig. 5a) and, subsequently, intercompares REMO and ROM in each forcing mode by
 492 illustrating the difference (REMO minus ROM) in the meridional temperature gradient at 925
 493 hPa (Fig. 5b). Our hypothesis is well-founded. Indeed, over the ocean and outside the latitude
 494 band of 20°-10°S and south of 38°S, REMO-ERA features a weaker meridional temperature
 495 gradient elsewhere across the ocean basin compared to ROM-ERA (Fig. 5b). A direct
 496 consequence is the reduced amount of captured moisture over the ocean per unit of time and
 497 its transport towards the Guinea Gulf due to weaker winds. This results in a drier Guinea Gulf
 498 in REMO-ERA compared to ROM-ERA (Fig. S2).



499

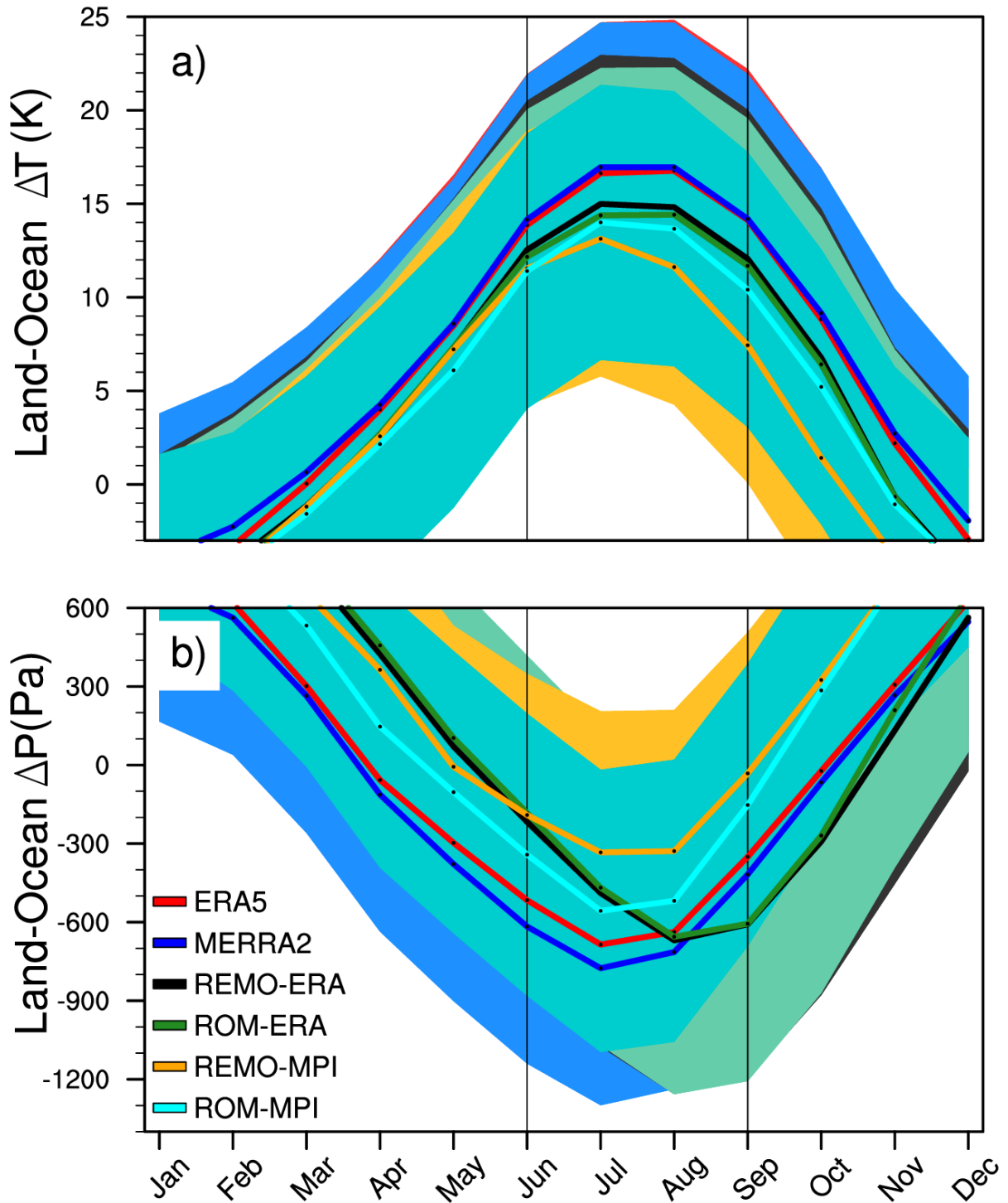
500 **Fig. 5** JAS climatology (1980-2005) of the latitudinal migration of the 925 hPa temperature gradient (a) and
 501 difference (b) (in 10^{-6}K/m) averaged over the longitudes 10°W - 10°E , from ERA5, MERRA2, REMO/ROM-ERA
 502 and REMO/ROM-MPI. The horizontal black bars delimit the latitudinal band 15° - 30°N and the vertical bar
 503 is the gradient value 0. The corresponding shaded area in color represents the standard deviation,
 504 indicating the variability in the temperature gradient.

505

506 Inland, although REMO-ERA exhibits a positive and stronger surface temperature
 507 gradient along the Guinean coast (0 - 10°N) compared to ROM-ERA, this difference is nearly

508 cancelled out over the Sahel region (10-20°N) with ROM-ERA's gradient slightly stronger than
509 that of REMO-ERA. Lower moisture availability in the Guinea Gulf in REMO-ERA relative to
510 ROM-ERA leads to weaker inland moisture penetration in REMO-ERA than in ROM-ERA,
511 conducive to a drier REMO-ERA over central and eastern Sahel. The positive thermal gradient
512 over the Guinea coast is a favorable condition for moisture depletion in the region. A similar
513 process may also be at play with the WAWJ, reducing precipitation in the western Sahel.
514 REMO-MPI shows a weaker meridional thermal gradient than ROM-MPI from the south up to
515 15°S, and then a stronger gradient almost elsewhere in the ocean basin (Fig. 5b). Over the
516 continent, REMO-MPI simulates a softly stronger surface temperature gradient than ROM-
517 MPI along the Guinean coast, which intensifies south of the Sahel (10-15°N). In contrast, north
518 of 15°N, the gradient reverses and becomes stronger in ROM-MPI from the northern Sahel
519 towards the Sahara (up to 30°N; Fig. 5b). The stronger thermal gradient in ROM-MPI over the
520 northern Sahel may have contributed to increased moisture influx into the interior of the
521 Sahel.

522 Figure 6 summarizes the changes in land-sea contrasts, including the thermal contrast
523 (ΔT , Fig. 6a) and the pressure contrast (ΔP , Fig. 6b). ΔT and ΔP are calculated as the differences
524 between land surface temperature and ocean SST, and land surface pressure and sea-level
525 pressure, respectively, between the Sahara continental mass (15°W-16°E; 20°-30°N) and the
526 eastern South Atlantic Ocean (15°W-16°E; 0-20°S). The (ΔT , ΔP) couple adequately reflects the
527 difference in rainfall between REMO and ROM. In fact, REMO-ERA and ROM-ERA, which
528 simulated similar rainfall amounts, also exhibit nearly identical ΔT and ΔP distributions.
529 Additionally, both reanalysis-forced experiments place the peak of ΔP in August instead of
530 July, as in the coupled cases, consistent with the one-month delay in the occurrence of
531 precipitation peak (Fig. 3). Conversely, REMO-MPI, which simulates a drier Sahel compared to
532 ROM-MPI, also simulates weaker temperature and pressure gradients than ROM-MPI. These
533 results suggest that the difference in the amount of advected moisture inland is responsible
534 for the spatial patterns of simulated rainfall in REMO and ROM. The differences in these
535 gradients leads to variations in the strength of the atmospheric circulation and monsoonal
536 flows and their penetration depth inland. These assumptions are discussed in the following
537 section.

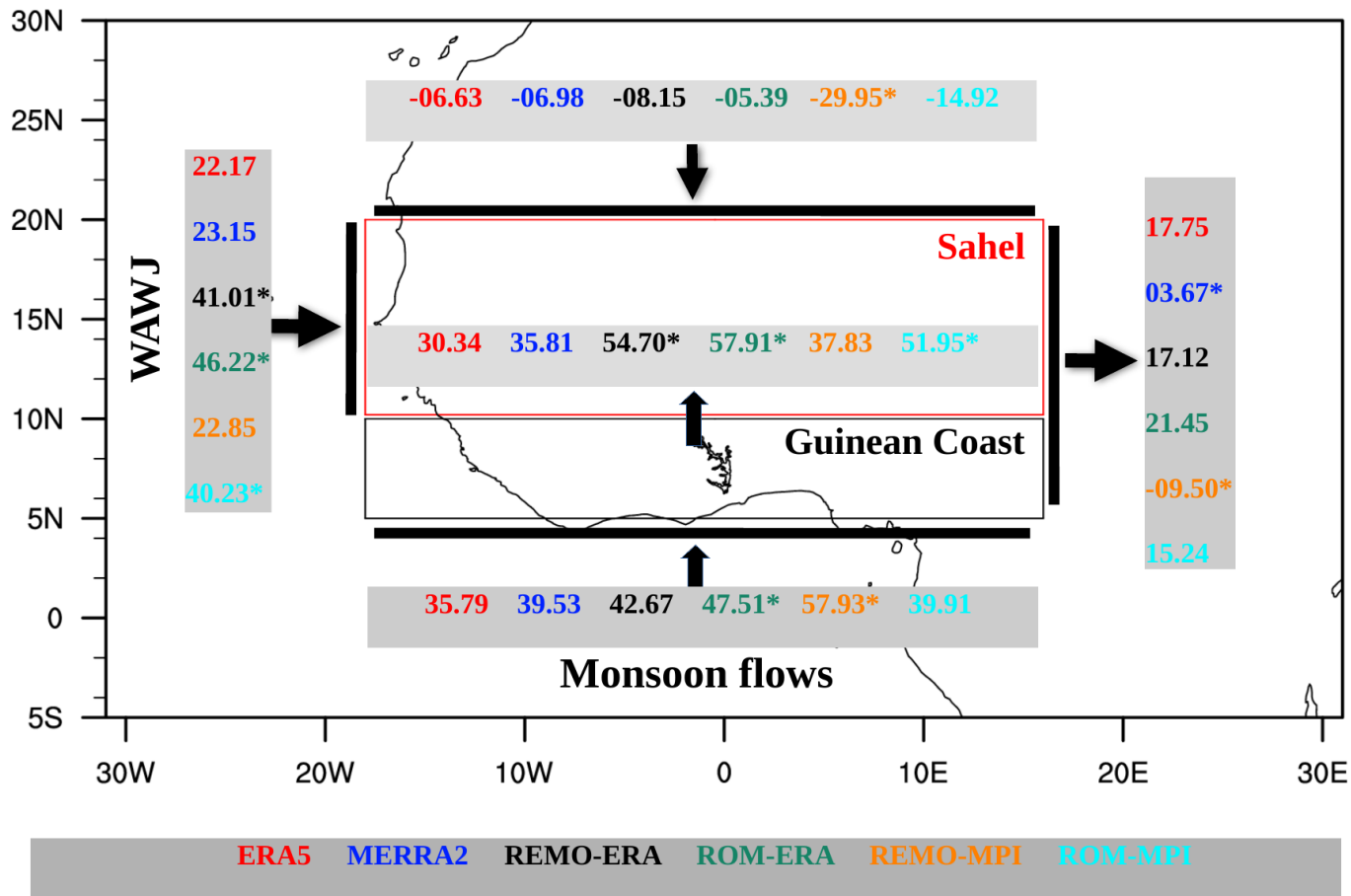


538
 539
 540
 541
 542
 543
 544
 545
 546

Fig. 6 Mean (1980-2005) seasonality of the near-surface **a)** land-ocean temperature difference (thermal contrast; ΔT in K) and **b)** land-surface pressure and ocean sea-level pressure difference (ΔP in Pa) between the interior of the continent (15°W-16°E, 20°-30°N) and the southeastern Atlantic Ocean (15°W-16°E, 0°-20°S), for the reanalyses ERA5 and MERRA2, and for REMO and ROM experiments. The corresponding shaded area in color represents the standard deviation, indicating the variability in ΔT (a) ΔP (b), respectively.

547 4.3 Low-level circulation response to coupling

548 Figure 7 shows the low-level circulation associated with the WAM rainfall climatology
549 in JAS. REMO-ERA and ROM-ERA, which exhibit quasi-similar WAM rainfall patterns, also
550 display similar low-level moisture transport (Fig. S6). The slightly drier nature of REMO-ERA
551 relative to ROM-ERA is strongly associated with their respective regional moisture
552 convergence in WA, and corroborates the assumptions formulated in section 4.2. Indeed, as
553 shown in Figure 7, REMO-ERA simulates lower monsoon flows ($42.67 \text{ kgm}^{-1}\text{s}^{-1}$) than ROM-ERA
554 ($47.51 \text{ kgm}^{-1}\text{s}^{-1}$) and a weaker moisture emanating from the WAWJ ($41.01 \text{ kgm}^{-1}\text{s}^{-1}$) than ROM-
555 ERA ($46.22 \text{ kgm}^{-1}\text{s}^{-1}$). Thus, ROM-ERA degrades the representativeness of monsoon fluxes, in
556 association with the deterioration in SSTs over the eastern equatorial Atlantic Ocean (Fig. S4)
557 and the deterioration in the accuracy in simulating the land-sea thermal and pressure
558 contrasts (Fig. 6). This has to be compared to a lower monsoon flow ($35.79 \text{ kgm}^{-1}\text{s}^{-1}$) and
559 WAWJ ($22.17 \text{ kgm}^{-1}\text{s}^{-1}$) in ERA5 than in ROM-ERA and REMO-ERA. ROM-MPI better simulates
560 the SSTs of the eastern tropical Atlantic Ocean than REMO-MPI (Fig. 4), resulting in an
561 improved simulation of monsoon fluxes ($39.91 \text{ kgm}^{-1}\text{s}^{-1}$) compared to ERA5 ($35.79 \text{ kgm}^{-1}\text{s}^{-1}$)
562 and MERRA2 ($39.53 \text{ kgm}^{-1}\text{s}^{-1}$) reanalyses, and relative to REMO-MPI ($57.93 \text{ kgm}^{-1}\text{s}^{-1}$). However,
563 the simulated transient fluxes through the northern boundary of the Guinean coast toward
564 the Sahel ($51.95 \text{ kgm}^{-1}\text{s}^{-1}$) as well as moisture supplied from through the WAWJ ($40.23 \text{ kgm}^{-1}\text{s}^{-1}$)
565 are degraded by the coupled ROM-MPI model compared to its atmosphere-only
566 counterpart, REMO-MPI (37.83 and $22.85 \text{ kgm}^{-1}\text{s}^{-1}$, respectively), which is closer to ERA5 and
567 MERRA2 reanalyses (30.35 and $35.81 \text{ kgm}^{-1}\text{s}^{-1}$, and 22.17 and $23.15 \text{ kgm}^{-1}\text{s}^{-1}$, respectively).
568



569
 570
 571
 572
 573
 574
 575
 576

Fig. 7 Low-level atmospheric moisture transport (1000-850 hPa) into the WA interior across each boundary. The numbers indicate the mean seasonal amount (1980-2005) of water vapor (in Kg/m/s) crossing each boundary, based on reanalysis datasets and REMO and ROM experiments. Asterisks (*) indicate the significance of values at 95% according to the *t* test. The black box represents the Guinean coast, and the red box represents the Sahel.

577 We put forward two hypotheses based on the aforementioned results: (1) equatorial
 578 east Atlantic Ocean SSTs influence the rainfall system through direct teleconnections over the
 579 Guinean coast, but indirectly in the Sahel, and the SST-Sahel rainfall relationships are not
 580 improved by coupling. This may explain why, under ESM-forced conditions, positive AV in the
 581 equatorial east Atlantic Ocean SSTs leads to positive precipitation AV along the Guinean coast
 582 but negative in the Sahel. (2) The modulating effect of SSTs on the Sahelian rainfall system is
 583 of secondary importance to local/regional forcing factors which are deteriorated by coupling.
 584 However, some of these local/regional factors, in return, respond to large-scale and even
 585 extratropical forcing factors. The accuracy of these factors could be either improved or
 586 degraded by coupling. Numerous studies have already demonstrated the modulating role of

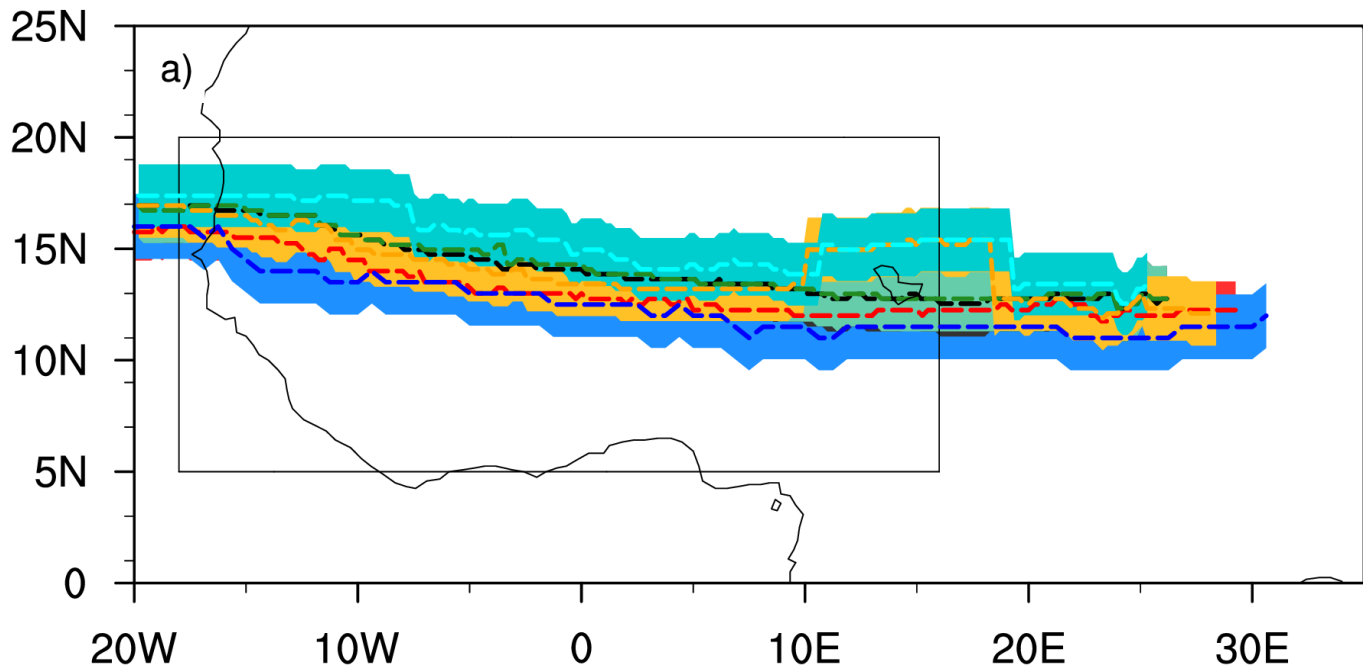
587 SSTs on Sahel rainfall (e.g., Zhao et al. 2005; Vizzy and Cook 2006; Giannini et al., 2013;
588 Rodríguez-Fonseca et al. 2015). For instance, Vizzy and Cook (2002) showed that anomalously
589 high SSTs in the Guinea Gulf lead to reduced rainfall in the Sahel but, conversely, increased
590 rainfall along the Guinean coast. This previous study is consistent with ours because, as found
591 in sections 3 and 4.1, the coupled ROM-MPI run attenuates the warm SST bias in the Guinea
592 Gulf as simulated by the uncoupled REMO-MPI run, which correlates with the drier behavior
593 of ROM-MPI along the Guinean coast but wetter in the Sahel (Fig. S2). This suggests that the
594 second hypothesis is more likely. As seen in Figure 7, we posit that stronger moisture fluxes
595 from the WAWJ and northward advection crossing the northern border of the Guinean coast
596 are responsible for the increased precipitation in the Sahel simulated by the ROM-MPI
597 coupled experiment. Consistently, Pu and Cook (2012) demonstrated that wet periods in the
598 Sahel feature enhanced westerly moisture advection originating from a strengthened WAWJ.
599 This leads to increased moisture availability in the Sahel's lower layer, thereby reducing the
600 atmospheric stability. The strengthening of inward flows in the Sahel through the northern
601 border of the Guinean coast is linked to an enhanced surface temperature gradient between
602 15°N and 30°N. In the next section, we examine whether the responses of other local/regional
603 factors of the WAM system to coupling are associated with the pattern of rainfall.

604 **4.4 AEJ and TEJ responses to coupling**

605 Two of the primary features of the WAM system are the AEJ and TEJ (Sultan and Janicot
606 2003; Nicholson 2013). The AEJ is the mid-tropospheric (700-600 hPa) response of the more
607 local and mesoscale features of the WAM system. While the AEJ is generated by an
608 increasing/decreasing meridional thermal/soil moisture gradient from the moistened Guinea
609 Gulf to the hot Sahara (Nicholson and Grist 2003; Cook 1999), it is primarily sustained by
610 surface heating, which generates dry convection in the Sahara thermal low region (Cook 1999;
611 Thorncroft and Blackburn 1999; Chen 2005). The passage of the AEJ is also associated with
612 disturbances known as African Easterly Waves (AEWs) with a periodicity ranging from 2 to 10
613 days and wavelengths ranging from 2 to 4×10^3 km, which develop through mixed baroclinic-
614 barotropic instability along the AEJ (Kiladis et al. 2006; Thorncroft et al. 2008). While analyses
615 based on AEWs are not conducted in this study due to the unavailability of daily simulation
616 data, conclusions can still be drawn from the analyses conducted on the AEJ. Wet conditions
617 in the Sahel are associated with a northward shift and weaker AEJ, conditions that favor

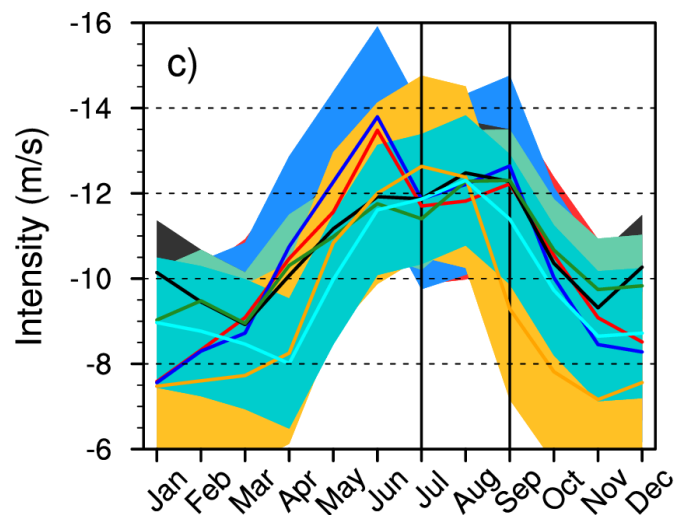
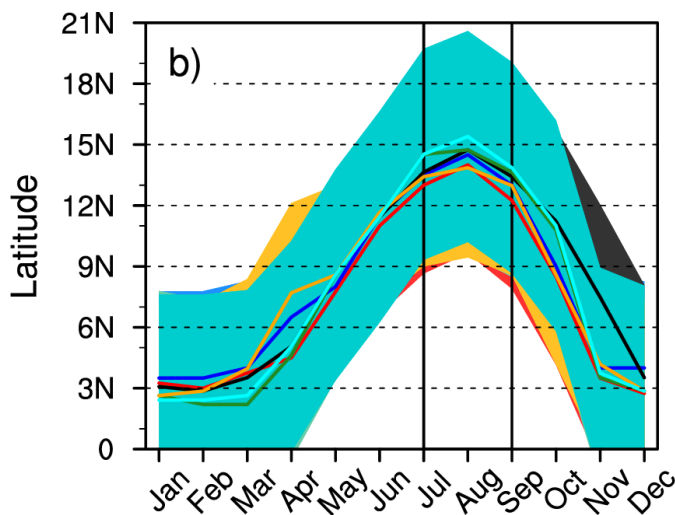
618 increased moisture convergence into the Sahel and subsequently, mesoscale convective
619 systems feeding convection (Nicholson and Grist 2003). The TEJ owes its existence to the
620 meridional thermal contrast between the Tibetan highlands and the Indian Ocean
621 (Koteswaram 1958). Numerous previous studies argued that in the Sahel, wet years exhibit a
622 strong TEJ, while dry years exhibit a weak TEJ, with a contrast that can reach a factor of two
623 (Nicholson and Grist 2003; Lemburg et al. 2019). Nicholson and Klotter (2020) questioned the
624 link between the TEJ and Sahel rainfall. They demonstrated that anomalously wet years can
625 occur without an anomalously strong TEJ. They argued that additional modelling studies are
626 needed to determine whether Sahel rainfall and the TEJ respond to the same forcing factors,
627 and that extratropical circulations control the TEJ via global SSTs.

628 Figure 8a,b shows that the coupled experiment ROM-MPI, which is moister over the
629 Sahel than its counterpart uncoupled REMO-MPI experiment, also shifts the core of the AEJ
630 northward. However, both experiments realistically represent the timing and latitudinal
631 migration of the jet. The coupling also improves the intensity of the AEJ in July and September
632 (Fig. 8c), in association with enhancement in the surface meridional temperature gradient
633 (Fig. S7). Once again, there are no important differences between the two reanalysis-forced
634 simulations, as they exhibit remarkably similar AEJ characteristics and surface thermal
635 gradients during the monsoon time. Figure S8 reveals that the coupling considerably improves
636 the AEJ and TEJ representation when simulations are forced with MPI-ESM-LR, although the
637 mean seasonal intensity remains slightly underestimated. A notable increase in magnitude
638 (Figs S8 and 9c) and an anomalous northward displacement (Fig. 9a,b) of the TEJ are evident
639 in the coupled ROM-MPI relative to REMO-MPI, and are consistent with the enhanced
640 precipitation over the Sahel. While the coupling affects the latitudinal-time positioning of the
641 TEJ (Fig. 9a,b), it significantly improves its intensity (Fig. 9c) and spatial pattern (Fig. S9). There
642 are also discrepancies in the longitudinal direction as simulated by the atmosphere-only
643 experiment REMO-MPI, which are resolved in the coupled ROM-MPI simulation (Fig. S9).
644 REMO-MPI strongly underestimates the TEJ over central equatorial Africa between 10°E and
645 30°E, a feature that is improved in the coupled ROM-MPI run.



646

— ERA5 — MERRA2 — REMO-ERA — ROM-ERA — REMO-MPI-ESM-LR — ROM-MPI-ESM-LR



647

— ERA5 — MERRA2 — REMO-ERA — ROM-ERA — REMO-MPI-ESM-LR — ROM-MPI-ESM-LR

648

649

Fig. 8 Long-term mean (1980-2005) JAS **a)** latitudinal-longitudinal location, **b)** latitudinal-time location (in °N) and **c)** intensity (m/s) of the mean core of the AEJ ($U\text{-wind} \leq -6$ m/s at 700 hPa), from reanalysis data ERA5 and MERRA2, and from REMO and ROM experiments. The corresponding shaded area in color represents the standard deviation, indicating the variability in both the AEJ location (a–b) and intensity (c).

650

The black box denotes WA.

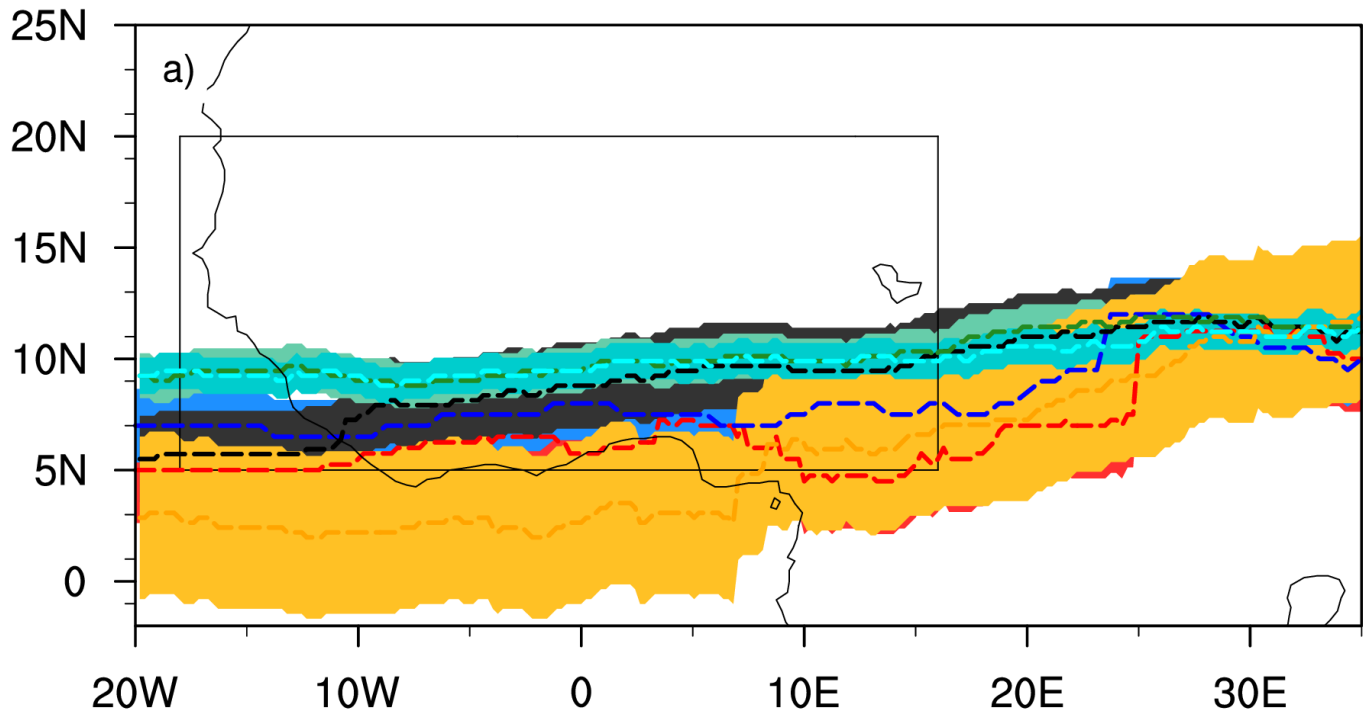
651

652

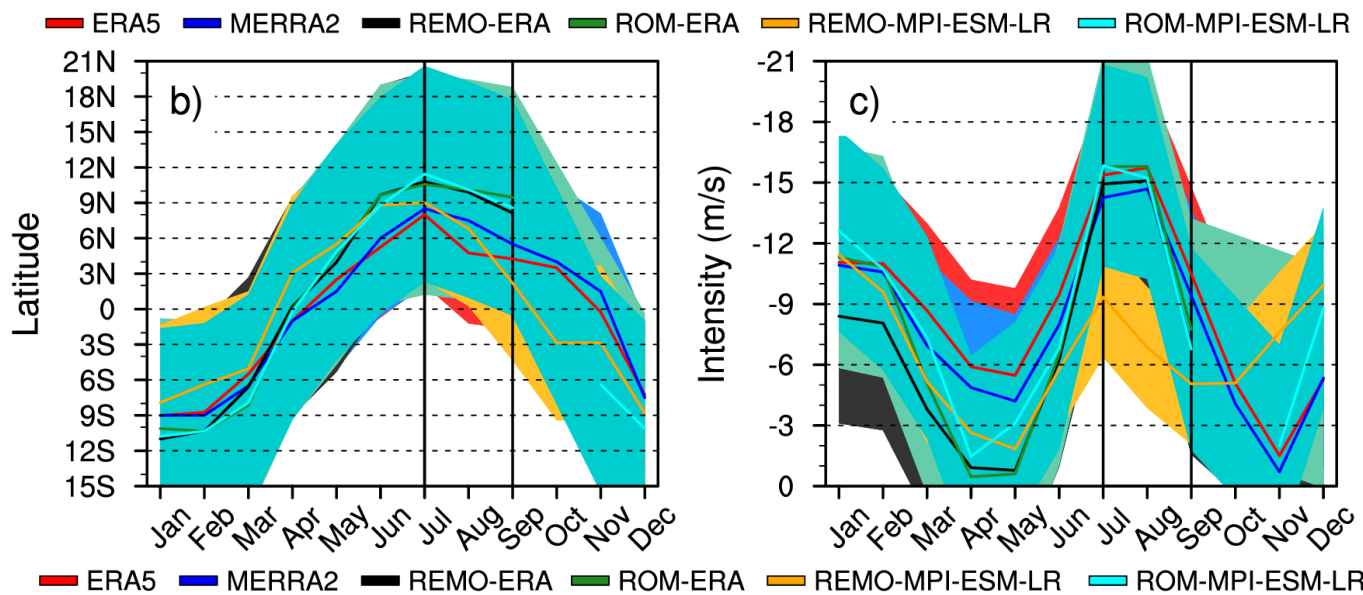
653

654

655



656



657

658

659 **Fig. 9** Long-term mean (1980-2005) JAS **a)** latitudinal-longitudinal location, **b)** latitudinal-time location
 660 (in °N) and **c)** intensity (m/s) of the mean core of the TEJ (U-wind ≤ -6 m/s around 200 hPa), from reanalysis
 661 data ERA5 and MERRA2, and from REMO and ROM experiments. The corresponding shaded area in color
 662 represents the standard deviation, indicating the variability in both the TEJ location (a–b) and intensity (c).
 663 The black box denotes WA.

664

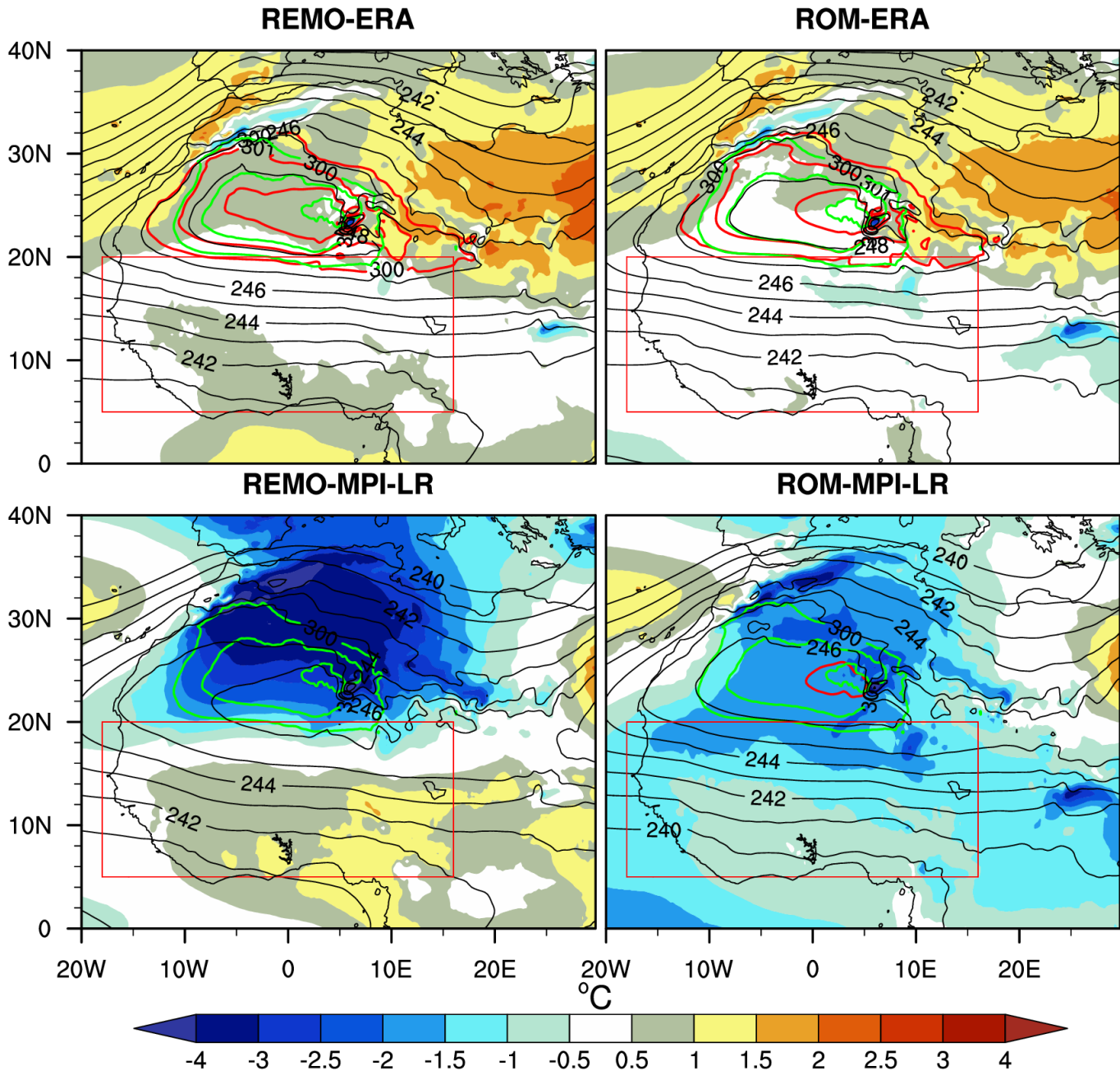
665 As AEWs are atmospheric disturbances related to the passage of the AEJ (Diedhiou et
 666 al., 1999; Thorncroft et al., 2008; Leroux and Hall, 2009), improvement of the AEJ offers
 667 potential insights into the simulation of AEWs (Tamoffo et al. 2022). In the present study, we

668 did not investigate the reasons behind the disparities in the simulated TEJ. However, the latest
669 study by Nicholson and Klotter (2020) sheds light on the drivers of TEJ, indicating that this
670 component of the WAM system is influenced by large-scale forcing factors. Due to the limited
671 area used in dynamical downscaling, accurately diagnosing these factors is challenging.
672 Nevertheless, differences between REMO-MPI and ROM-MPI in simulating the TEJ stands out
673 (Fig. S9), whereas differences are smaller for the AEJ (Fig. S8). This suggests that the coupling
674 configuration employed in this study improves the TEJ's strength more than the AEJ's
675 strength, especially in terms of intensity. This result aligns with the recent arguments made
676 by Nicholson and Klotter (2020) that the TEJ is heavily influenced by extratropical factors,
677 which act through global SSTs. The global nature of the oceanic component of ROM, MPIOM,
678 contributes to enhancing the accuracy of SSTs in the ocean basins that drive the TEJ. However,
679 it's important to note that the coupling has led to improvements in the intensity of both jets,
680 leaving the debate solely on the too-northward shifting of their cores as opposed to
681 reanalyses. A work by Whittleston et al. (2017) also emphasized the lack of a jet-rainfall
682 relationship in climate models over the West African Sahel. Furthermore, as previously
683 mentioned, the overall condition of the jets aligns with increased rainfall over the Sahel,
684 resulting in negative *AV*. The coupled ROM-MPI run indicates that the degraded or
685 unimproved rainfall climatology over the Sahel can be primarily attributed to biases in regional
686 or local WAM's forcing factors.

687 **4.5 The SHL's response to coupling**

688 Figure 10 allows assessing the assumptions from section 4.3 and demonstrates that
689 the inadequate representation of the SHL is not associated with the negative *AV* over the
690 Sahel. Instead, it points to the overestimated WAWJ and northward low-level cross-northern
691 border Guinean coast flows as potential contributing factors. Indeed, the SHL is detected
692 through the 850 hPa temperature climatology (Lavaysse, 2015) and the low-level atmospheric
693 thickness (LLAT), i.e., the difference in geopotential heights between 700 and 925 hPa
694 (Lavaysse et al., 2009). Both REMO-ERA and ROM-ERA exhibit similar biases in the SHL
695 compared to ERA5, consistent with the similarities in their simulated rainfall patterns in the
696 Sahel (Fig. S2). However, while the coupling in ROM-MPI brings significant improvements in
697 the representation of SHL (previously strongly underestimated by REMO-MPI by $\sim 4^{\circ}\text{C}$), the
698 strength of the thermal depression remains lower than that simulated by ERA5 ($\sim 2^{\circ}\text{C}$). Thus,

699 the ESM-forced simulations underestimate the magnitude of the SHL. A similar conclusion is
 700 reached using LLAT (Fig. 10).

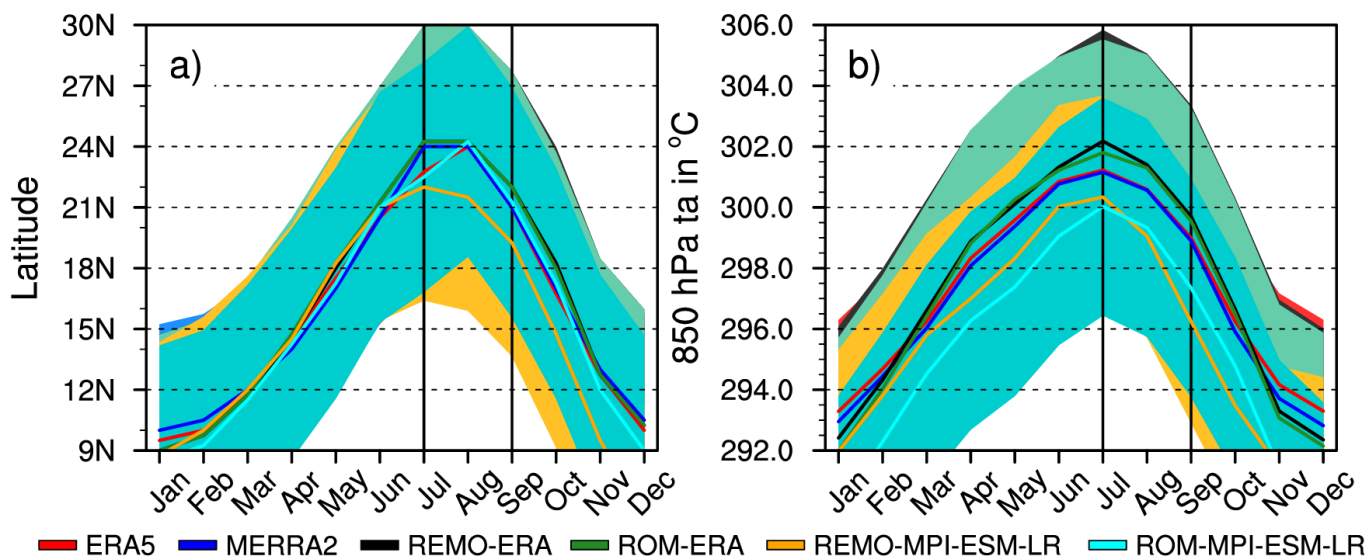


701
 702
 703
 704
 705
 706
 707
 708
 709

Fig. 10 Mean JAS seasonal Sahara heat low (SHL) bias (REMO/ROM minus ERA5) highlighted by mean JAS 850 hPa temperature (in °C, shaded). The red contour line represents the heat low location in the analyzed dataset, while the green contour line represents the heat low location in ERA5 (used as a reference dataset), using ≥ 300 -K temperature contours. Black contours are the low-level atmospheric thickness (LLAT; in meters), i.e., the difference in geopotential heights between 700 and 925 hPa (Lavaysse et al., 2009). The red boxes indicate the WA region.

710 Regarding the latitudinal displacement during the monsoon period (Fig 11a), the two
 711 simulations driven by ERA-Interim remain pretty similar, while in the simulations driven by the
 712 ESM MPI-ESM-LR, the coupling improves the latitudinal positioning of the SHL, with ROM-MPI
 713 following the ERA5 curve closely. Here, the enhancement consisted of shifting the SHL's core
 714 further north, in line with the increased rainfall over the Sahel (Lavaysse et al. 2010; Dixon et
 715 al. 2017). Figure 11b shows that the reanalysis-forced runs simulate a stronger SHL than the
 716 ERA5 throughout the monsoon season. Contrastingly, REMO-MPI and ROM-MPI simulate a
 717 weaker SHL. Notably, ROM-MPI tends to improve REMO-MPI, especially in August and
 718 September, consistent with improvements in the AEJ during the same monsoon months (Fig.
 719 8c).

720



721
722

Fig. 11 (a) The mean latitudinal location of the heat low during the July-August-September months, defined as the point of the maximum zonal mean (18°W-16°E) 850 hPa air temperature, localised over the latitudes 0°-35°N; **(b)** the mean intensity of the heat low, defined as the temperature recorded at the point of 850 hPa air temperature maximum. The corresponding shaded area in color represents the standard deviation, indicating the variability in both the heat low location (a) and intensity (b). The black bars denote the July-August-September months.

729

730 Previous research supports the plausibility of the aforementioned findings. For
 731 instance, ROM-MPI models a stronger SHL than REMO-MPI, in accordance with its higher land-
 732 ocean thermal contrast (∇T) compared to that of REMO-MPI (Biasutti et al. 2009). Despite the
 733 fact that the coupling enhances the SHL in association with improvements in the east
 734 equatorial Atlantic Ocean SSTs, its strength remains persistently underestimated. This result

735 supports the earlier conclusion of Dixon et al. (2017), who reported that the modulating
736 effects of SSTs on the features of the SHL's climatology are secondary to those of atmospheric
737 biases. Several studies argued that the strength of the SHL is influenced by variability in the
738 local radiative budget, which, in turn, is associated with large-scale processes (Vizy and Cook
739 2009; Chauvin et al. 2010; Lavaysse et al. 2010; Dixon et al. 2017). Indeed, the process
740 generally involves cooling/warming of the Sahara and, consequently, the SHL region, through
741 advection of cold/warm air from mid-latitude waves (Chauvin et al. 2010) or Mediterranean
742 regions (Vizy and Cook 2009). The local radiative budget may also be modified by advected
743 moist air over the SHL (Engelstaedter et al. 2015) and by dust transported by atmospheric
744 circulation (Lavaysse et al. 2011; Schepanski et al. 2017).

745 Figure S10 illustrates that effectively, biases in the radiative budget largely account for
746 the biases in the strength of the SHL. Reanalysis-forced runs, which slightly overestimate the
747 strength of the SHL, simulate slight negative biases (-10.55 and -9.23 Wm^{-2}) in the net surface
748 solar radiation (NSSR). Conversely, REMO-MPI and ROM-MPI, which underestimate the
749 strength of the SHL, strongly underestimate the NSSR (-23.65 and -19.97 Wm^{-2} , respectively).
750 Furthermore, the difference between REMO-MPI and ROM-MPI (up to -3.68 Wm^{-2}) reveals
751 that the improvement provided by the coupled ROM-MPI model is associated with the
752 enhancement in the NSSR, which has mitigated the magnitude of negative biases. The
753 investigation into the reasons behind changes in the local radiative budget over the SHL's
754 region is reserved for forthcoming research. The outstanding question is whether the
755 climatology of simulated precipitation over the Guinean Coast and Sahel, in response to
756 changes in moisture availability, is preceded by atmospheric instability/stability conditions
757 associated with convection.

758 **4.6 Atmospheric instability response to coupling**

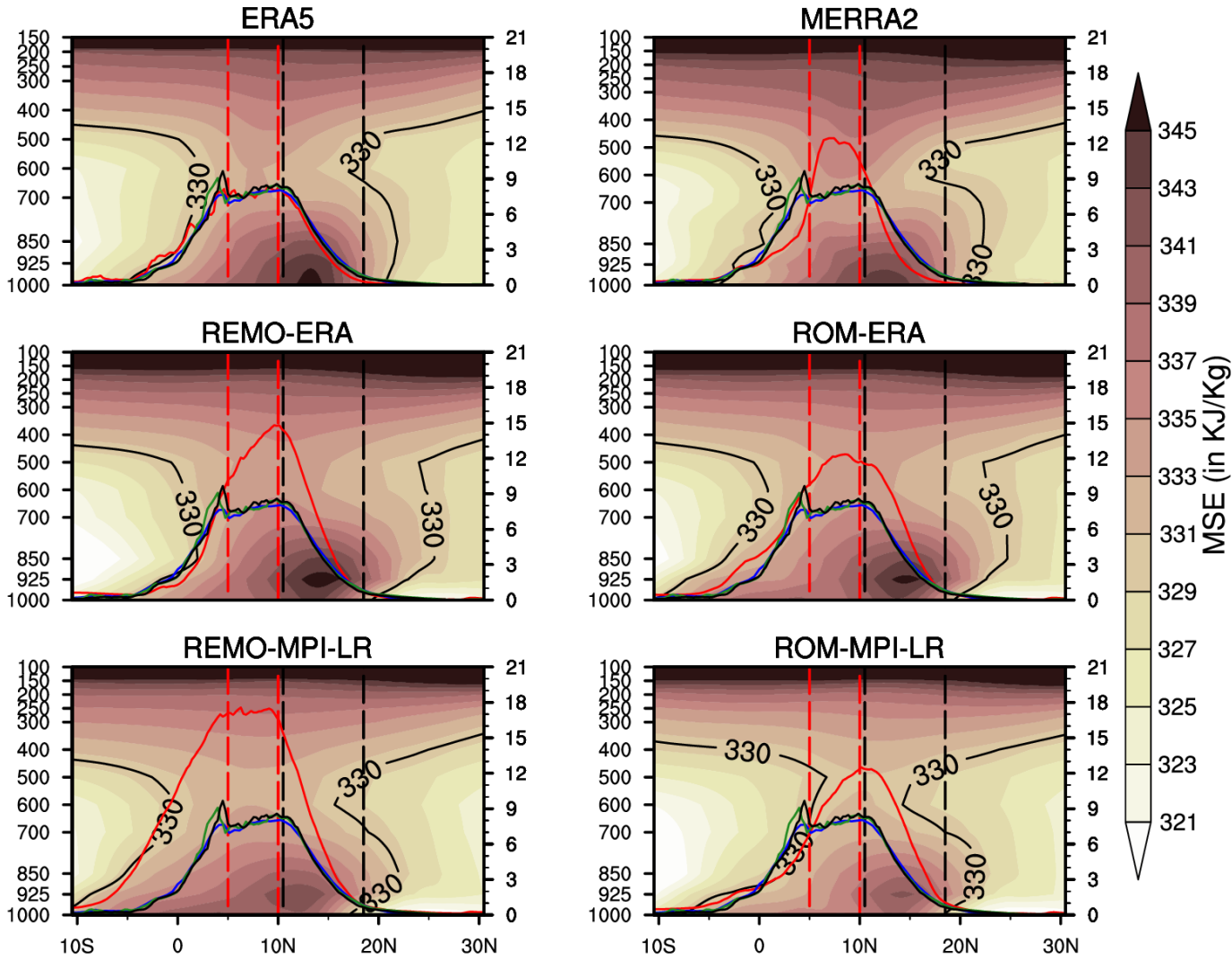
759 Ninety percent of precipitation over the Sahel originates from mesoscale convective
760 systems (MCSs; Nesbitt et al. 2006), highlighting the crucial role of convection in modulating
761 the region's rainfall pattern. Given this perspective, it is necessary to investigate how
762 modifications in the atmospheric circulation, in response to the coupling, induce changes in
763 atmospheric instability. We utilized the moist static energy (MSE) thermodynamic metric,
764 which facilitates the connection between atmospheric circulation with regional or local
765 moisture availability. Through the use of MSE, we examined the atmospheric instability or

766 stability associated with the climatology of rainfall, as modelled by each experiment. The MSE
767 is defined as shown in Equation 3:

$$768 \quad \quad \quad MSE = c_p T + gz + Lq \quad \quad \quad (3)$$

769 with the first two terms on the right-hand side representing the dry static energy (DSE;
770 $DSE = c_p T + gz$) input; $c_p T$ is the sensible heat, gz is the potential energy and Lq is the latent
771 static energy (LSE; $LSE = Lq$); c_p is the specific heat at constant pressure, T is the air
772 temperature, g is the gravitational constant, z is the geopotential height, L is the latent heat
773 of condensation and q is the specific humidity. To emphasize the difference in instability or
774 stability between experiments, we estimate, for each run, the latitudinal average (between
775 5° - 10° N for the Guinea Coast and 10° - 20° N for the Sahel) of MSE, integrated from 1000 to 700
776 hPa. From Figure 12, a number of consistencies emerge across all the datasets, (1) the WA is
777 a convectively unstable region, as the MSE profile weakens with the elevation; (2) in the Sahel
778 region, the convection is initiated by strong instability in the lower layers (<800 hPa) where
779 the availability of MSE and specific humidity (Fig. S11) is high; (3) there is also agreement that,
780 conversely, stronger instability (high MSE) is not conducive to high rainfall, as wetter
781 experiments (coupled runs) simulate weaker MSE compared to drier experiments
782 (atmosphere-only runs), with a REMO minus ROM mean difference $>0.50 \text{ KJkg}^{-1}$ for reanalysis-
783 forced runs, and $>0.90 \text{ KJkg}^{-1}$ for the ESM-forced runs. However, REMO-MPI, which was found
784 to be moister over the Guinean coast than ROM-MPI, also simulates a stronger MSE over the
785 Guinean coast, with a difference REMO minus ROM $>3.70 \text{ KJkg}^{-1}$. Moreover, REMO-ERA and
786 ROM-ERA, displaying nearly equal rainfall amounts over this region, also simulate similar MSE
787 with a REMO minus ROM difference $<0.50 \text{ KJkg}^{-1}$. This suggests that over the Guinean coast,
788 strong MSE indeed leads to strong precipitation. The LSE (Fig. S12) appears to be the
789 component linking MSE and precipitation, as the overall datasets mirror similar variations in
790 DSE (Fig. S13). The surplus of low-level moisture content, originating from the WAWJ and the
791 northward low-level cross-northern border Guinean coast influx (Figs 7 and S6), destabilizes
792 the near-surface layers over the Sahel. Simultaneously, radiative cooling resulting from
793 enhanced evaporation (Fig. S5) weakens low-level temperatures, thereby attempting to
794 stabilize the lower layers of the troposphere. Previous studies also reported similar results
795 (Giannini 2010; Patricola and Cook 2007). The weakening in MSE, as modelled by ROM-MPI,
796 agrees with the lowering in equatorial east Atlantic Ocean SSTs, which is associated with the

797 reduction in the advected meridional MSE entering the Sahel via the northern frontier (Hill et
 798 al. 2017).



799
 800

801 **Fig. 12** Latitude-height cross-sections of the mean JAS moist static energy (MSE; kJ/kg). Data used are from
 802 reanalysis ERA5 and MERRA-2 datasets, and the REMO and ROM experiments over the period 1980-2005.
 803 The 330-KJ/Kg contour highlights the potential zone of the convection band. The red line is the latitudinal
 804 migration of the rainband (mm/day) from the dataset under consideration while the blue, green and black
 805 denote the rainband from CRU.ts.05, GPCC-v2020 and CHIRPS2 observations. The red bars highlight the
 806 latitudinal band of the **Guinea Coast** (5°-10°N) while the black bars highlight the latitudinal band of the
 807 **Sahel** (10°-20°N).
 808

809 **5. Summary and concluding discussion**

810 Preliminary studies (e.g. Paxian et al. 2016) showed that dynamical downscaling of
 811 coupled global ocean-regional atmosphere RCMs may enhance the simulation of WAM
 812 rainfall. The present study aimed to shed light on how such coupling adds value to WAM
 813 rainfall, focusing the analyses on the mean climatology and providing a thorough analysis of

814 the West African monsoon system. We evaluated the processes underlying the calculated
815 added value (AV) of including coupling. Additionally, we aimed at understanding how changes
816 in eastern equatorial Atlantic Ocean SSTs force the WAM system or, alternatively, how prior
817 changes in the WAM system induce potential oceanic responses. To achieve this, we utilized
818 the results of dynamical downscaling at $\sim 25\text{-km}$ horizontal resolution from two versions of the
819 AWI-GERICS RCM model: the atmosphere-only version REMO and the coupled global ocean-
820 regional atmosphere ROM version. The main findings can be summarized as follows:

- 821 1. The results are not sensitive to the reference datasets (CRU.ts4.05,
822 GPCP.v2020, CHIRPS2, and ERA5). The results are quite similar for the
823 reanalysis-forced runs (REMO-ERA and ROM-ERA), and the strongest
824 differences occur in the ESM-forced experiments (REMO-MPI and ROM-MPI).
825 REMO-ERA and ROM-ERA are wetter than the overall reference data in most
826 parts of WA, while REMO-ERA is slightly drier than ROM-ERA. When driven by
827 MPI-ESM-LR, the spatial pattern of AV consists of a dipole-like structure, with
828 enhancements over much of the Guinea Coast (around $88\% \pm 2.52\%$) and a
829 small part of south-central and western Sahel ($\sim 10\% \pm 2.75\%$), and then
830 degradations over almost half of the Sahel ($46\% \pm 3\%$). Also, under this mode,
831 REMO and ROM show equivalent performance over $40\% \pm 3.41\%$ of the Sahel.
832 In this context, REMO and ROM are both moister than the overall reference
833 datasets in most parts of WA, but REMO is wetter (drier) than ROM over the
834 Guinean coast (Sahel). Additionally, coupling enhances the ITCZ and the WAM
835 rain-band intensity and more broadly, improves the interlinkages between
836 SSTs and monsoon fluxes under ESM-forced conditions compared to
837 reanalysis-forced conditions.
- 838 2. Without the influence of biased boundary conditions, ocean coupling
839 exacerbates SST biases over the eastern equatorial Atlantic Ocean, with a
840 knock-on effect on the associated atmospheric fields. However, in the ESM-
841 forced mode, the coupling instead ameliorates the representation of SSTs over
842 this ocean basin, in mitigating the warm SST biases inherited from the driving
843 ESM MPI-ESM-LR.

844 3. Improvements of the eastern equatorial Atlantic Ocean SSTs lead to
845 improvements in the intensity of monsoon fluxes, achieved through better
846 simulations of evaporation and atmospheric circulation. Indeed, in response to
847 the lowering in warm SST biases, the coupled experiment ROM-MPI also
848 weakens the evaporation over the ocean basin. This leads to decreased
849 amounts of overestimated moisture transported towards the Guinean Gulf, as
850 simulated by the uncoupled REMO-MPI, but still higher compared to ERA5.

851 4. The coupling also leads to improvements in the representation of land-sea
852 thermal and pressure contrasts (ΔT , ΔP), resulting in enhancements in the
853 simulation of the strength of the monsoon flows. Specifically, the weakening in
854 warm SST biases over the Guinean Gulf strengthens the land-sea thermal
855 contrast and amplifies the pressure contrast between the Sahara and the
856 Guinean Gulf. However, moisture fluxes entering the Sahel are overestimated
857 due to the higher-than-observed northward low-level cross-northern border
858 Guinean coast flows, which are related to the stronger surface temperature
859 gradient between 15°-30°N, and because of the overestimated WAWJ. As a
860 result, the positive ROM-MPI's AV over the Guinean coast is associated with
861 enhancements in the monsoon flows, but the improvement is mitigated by a
862 stronger moisture divergence across the northern boundary into the Sahel.
863 Conversely, its negative AV over the Sahel is a result of the overestimated
864 moisture convergence from the Guinean coast and the WAWJ.

865 5. Coupling improves the representation of the intensity of the mid- (700-600
866 hPa) and upper-tropospheric circulation (around 200 hPa). Indeed, the coupled
867 experiment ROM-MPI enhances the magnitude of the AEJ, along with
868 improvements in the intensity and latitudinal positioning of its maintenance
869 mechanism, the SHL. In turn, the SHL is improved in association with the
870 reduction in the magnitude of negative biases in the Saharan radiative budget,
871 and the enhancement in the land-sea thermal contrast. The intensity of the TEJ
872 is also significantly enhanced, likely due to a better representation of SSTs in
873 ocean basins that influence the TEJ (Nicholson and Klotter 2020), as modelled
874 by the global ocean model MPIOM. However, the coupling shifts the latitudinal

875 positioning of the jets too far north, which is consistent with increased rainfall
876 over the Sahel leading to negative AV.

877 6. There is consistency among the overall datasets in terms of convection being
878 triggered in the lower layers of the troposphere (<800 hPa), where the MSE
879 and specific humidity are maximized. Additionally, there is agreement that the
880 LSE is the component of the MSE that plays a crucial role in linking it to
881 precipitation. However, in uncoupled experiments, the modelled MSE over the
882 Sahel is stronger in comparison to the corresponding coupled simulations.
883 Conversely, in coupled runs, the Sahel experiences more rainfall than in
884 uncoupled runs. This suggests that convection in the Sahel is associated with
885 moderated instability. A similar analysis conducted over the Guinean coast
886 shows that higher instability, on the other hand, leads to stronger ascent
887 motions, consequently resulting in increased precipitation. As simulated by the
888 coupled experiment ROM-MPI, it is logical that the overestimated evaporation
889 over most parts of the Sahel contributes to increased radiative cooling through
890 the evaporative cooling due to a larger latent heat flux, thereby strengthening
891 the stability of the lower layers through a weakening in temperature at those
892 levels. Similarly, the MSE may also weaken in response to the reduction in
893 equatorial east Atlantic Ocean SSTs, presumably inducing a decrease in the
894 advected meridional MSE entering the Sahel through its northern boundary.

895 7. Compared to their atmosphere-only counterparts, the coupled experiments
896 exhibit a stronger surface temperature gradient, located around 20°N for ROM-
897 ERA and within the latitude band of 15°-30°N for ROM-MPI. Proportionally,
898 these thermal gradients are responsible for stronger moisture advection into
899 the Sahel when compared not only to their respective uncoupled counterparts
900 but also in relation to reanalyses. The strength of this surface temperature
901 gradient drives the northward extent of the WAM rain-band as it defines the
902 depth of inland penetration of monsoon fluxes. Consequently, the latitudinal
903 positioning of the WAM convective system is determined by the force of this
904 surface thermal gradient, which, in turn, controls the intensity of convective
905 activities and the strength of monsoon flows. Thus, the monsoon fluxes can be
906 understood as a product of the WAM convective system. In other words, while

907 the reversal in the land-sea thermal contrast triggers the monsoon fluxes over
908 the ocean basin, it is the surface temperature gradient between the Sahara and
909 the Sahel that maintains inflows towards the Sahel, thereby regulating the
910 amount and depth of inland moisture convergence. Similar conclusions were
911 reached by Birch et al. (2014) using explicit simulations. These authors
912 demonstrated that convective activity forces the monsoon winds through the
913 pressure gradient between the Guinea coast and the Sahel, in association with
914 low pressure in the Sahel. These conditions are favored by the intensification
915 of the SHL as modelled by ROM-MPI compared to REMO-MPI.

916 The present study further demonstrates the need of simulating monsoon systems
917 using climate models that consider all earth system components involved. Indeed, these
918 findings show that under certain conditions, significant biases in large-scale processes can
919 obscure local/regional factors, which have a predominant imprint on the local/regional
920 climate system. For instance, excessively warm modelled SSTs over the Guinea Gulf tend to
921 hide the surface thermal gradient between 15°N-30°N, which is responsible for sustaining
922 monsoon flows. This argument is even more valid since compared to the reanalysis ERA5, the
923 coupled ROM-MPI run has significantly improved the representativeness of this surface
924 thermal gradient, unlike the atmosphere-only REMO-MPI run. Whether we elucidated the
925 reason behind the stronger-than-actual northward low-level cross-northern border Guinean
926 coast moisture fluxes towards the Sahel, as modelled by the coupled experiment ROM-MPI,
927 the causes of overestimated moisture originating from the WAWJ are still lacking and will
928 prompt forthcoming research.

929 It is worth noting that the robustness of these results must be further assessed since
930 our study focuses only on the results of a single dynamically downscaled ESM through an RCM
931 in both its coupled and uncoupled configurations. Further analyses should involve other RCMs
932 in both configurations, forced with different ESMs. However, we advocate in advance for the
933 greater reliability of the coupled model, ROM, over the uncoupled model, REMO. ROM has
934 demonstrated advantages in modelling other monsoon systems such as the East Asian
935 summer monsoon (Zhu et al., 2020), CORDEX Central America (Cabos et al., 2018), Central
936 Africa (Weber et al., 2022; Tamoffo et al., 2024), and the northern North Atlantic and Europe
937 (Sein et al., 2015). Likewise, comparing REMO and ROM forced by the AMIP and CMIP versions
938 of MPI-ESM could provide further insight into the impact of coupling on the simulation of the

939 WAM. These experiments will allow for a few decades of spin-up, reducing possible
940 differences related to the spin-up time length. In this regard, ERA5, which extends back to
941 1940, could also be utilized.

942

943 **Acknowledgements**

944 The research of this article was supported by the Humboldt-Stiftung as part of the Humboldt
945 Research Fellowship for researchers of all nationalities and research areas: postdoctoral and
946 experienced researchers programme. The Helmholtz-Zentrum Hereon has funded the Open
947 access. The model simulations were performed at the German Climate Computing Center
948 (Deutsches Klimarechenzentrum, DKRZ) in Hamburg, with the support of the Climate Service
949 Center Germany (GERICS). We acknowledge all the reanalysis, satellite and observational data
950 providers used in this study. The helpful input of Peter Hoffmann was also really appreciated.
951 The authors thank the three anonymous reviewers and the editor whose comments helped
952 improve and clarify this manuscript.

953 **Competing Interests.** The authors declare no conflicts of interest relevant to this study.

954

955 **Data Availability Statement**

956 The model simulations were performed at the German Climate Computing Center
957 (Deutsches Klimarechenzentrum, DKRZ) in Hamburg. All observational and reanalysis data
958 used in this study are publicly available at no charge and with unrestricted access. The ERA5
959 reanalysis is produced within the Copernicus Climate Change Service (C3S) by the ECMWF
960 and is accessible via the link [https://cds.climate.copernicus.eu/cdsapp#!/dataset/reanalysis-
era5-pressure-levels-monthly-means?tab=1/4form](https://cds.climate.copernicus.eu/cdsapp#!/dataset/reanalysis-era5-pressure-levels-monthly-means?tab=1/4form); the MERRA2 reanalysis, developed by the
962 NASA, is available online (at [https://disc.gsfc.nasa.gov/datasets?keywords=1/4%22MERRA-
2%22&page=1/41&source=1/4Models%2FAnalyses%20MERRA-2](https://disc.gsfc.nasa.gov/datasets?keywords=1/4%22MERRA-2%22&page=1/41&source=1/4Models%2FAnalyses%20MERRA-2)). The GPCP observational
964 data set is available at [https://opendata.dwd.de/climate_environment/GPCP/html/fulldata-
monthly_v2020_doi_download.html](https://opendata.dwd.de/climate_environment/GPCP/html/fulldata-monthly_v2020_doi_download.html). the CRU-v4.04 dataset is available at
966 https://data.ceda.ac.uk/badc/cru/data/cru_ts/cru_ts_4.05/data/pre (UEA, 2019); the
967 CHIRPS2 data are available at [https://data.chc.ucsb.edu/products/CHIRPS-
2.0/global_daily/netcdf/](https://data.chc.ucsb.edu/products/CHIRPS-2.0/global_daily/netcdf/).

969

970 **References**

971 Akinsanola, A. A., Ajayi, V. O., Adejare, A. T., Adeyeri, O. E., Gbode, I. E., Ogunjobi, K. O., ...
972 Abolude, A. T. (2017). Evaluation of rainfall simulations over West Africa in dynamically
973 downscaled CMIP5 global circulation models. *Theoretical and Applied Climatology*, 132(1–2),
974 437–450. <https://doi.org/10.1007/s00704-017-2087-8>

975

976 Akinsanola, A.A., Zhou, W. Projections of West African summer monsoon rainfall extremes
977 from two CORDEX models. *Clim Dyn* 52, 2017–2028 (2019). [https://doi.org/10.1007/s00382-](https://doi.org/10.1007/s00382-018-4238-8)
978 [018-4238-8](https://doi.org/10.1007/s00382-018-4238-8)

979

980 Biasutti, M., Sobel, A. H., & Camargo, S. J. (2009). The role of the sahara low in summertime
981 sahel rainfall variability and change in the CMIP3 models. *Journal of Climate*, 22(21), 5755–
982 5771. <https://doi.org/10.1175/2009jcli2969.1>

983

984 Biasutti, M. (2019). Rainfall trends in the African Sahel: Characteristics, processes, and
985 causes. *WIREs Climate Change*, 10(4). <https://doi.org/10.1002/wcc.591>

986

987 Bichet A, Diedhiou A, Hingray B, Evin G, Touré NE, Browne KN, Kouadio K (2020) Assessing
988 uncertainties in the regional projections of precipitation in CORDEX AFRICA. *Clim Change*
989 162(2):583–601. <https://doi.org/10.1007/s10584-020-02833-z>

990

991 Birch, C. E., Parker, D. J., Marsham, J. H., Copsey, D., & Garcia-Carreras, L. (2014). A seamless
992 assessment of the role of convection in the water cycle of the West African Monsoon.
993 *Journal of Geophysical Research: Atmospheres*, 119(6), 2890-2912.

994 <https://doi.org/10.1002/2013jd020887>

995

996 Boone, A., de Rosnay, P., Balsamo, G., Beljaars, A., Chopin, F., Decharme, B., Xue, Y. (2009).
997 The AMMA land surface model intercomparison project (ALMIP). *Bulletin of the American*
998 *Meteorological Society*, 90(12), 1865–1880. <https://doi.org/10.1175/2009bams2786.1>

999

1000 Boone, A. A., Pocard-Leclercq, I., Xue, Y., Feng, J., & de Rosnay, P. (2010). Evaluation of the
1001 WAMME model surface fluxes using results from the AMMA land-surface model
1002 intercomparison project. *Climate Dynamics*, 35(1), 127–142.
1003 <https://doi.org/10.1007/s00382-009-0653-1>
1004
1005 Cabos, W., Sein, D. V., Pinto, J. G., Fink, A. H., Koldunov, N. V., Alvarez, F., ... Jacob, D. (2016).
1006 The South Atlantic Anticyclone as a key player for the representation of the tropical Atlantic
1007 climate in coupled climate models. *Climate Dynamics*, 48(11–12), 4051–4069.
1008 <https://doi.org/10.1007/s00382-016-3319-9>
1009
1010 Cabos, W., Sein, D. V., Durán-Quesada, A., Liguori, G., Koldunov, N. V., Martínez-López, B., ...
1011 Pinto, J. G. (2018). Dynamical downscaling of historical climate over CORDEX Central
1012 America domain with a regionally coupled atmosphere–ocean model. *Climate Dynamics*,
1013 52(7–8), 4305–4328. <https://doi.org/10.1007/s00382-018-4381-2>
1014
1015 Cabos, W., de la Vara, A., Álvarez-García, F. J., Sánchez, E., Sieck, K., Pérez-Sanz, J.-I., ... Sein,
1016 D. V. (2020). Impact of ocean-atmosphere coupling on regional climate: The Iberian
1017 Peninsula case. *Climate Dynamics*, 54(9–10), 4441–4467. [https://doi.org/10.1007/s00382-](https://doi.org/10.1007/s00382-020-05238-x)
1018 [020-05238-x](https://doi.org/10.1007/s00382-020-05238-x)
1019
1020 Chauvin, F., Roehrig, R., & Lafore, J.-P. (2010). Intraseasonal variability of the saharan heat
1021 low and its link with midlatitudes. *Journal of Climate*, 23(10), 2544–2561.
1022 <https://doi.org/10.1175/2010jcli3093.1>
1023
1024 Chen, T.-C. (2005). Maintenance of the midtropospheric north African summer circulation:
1025 Saharan high and African easterly jet. *Journal of Climate*, 18(15), 2943–2962.
1026 <https://doi.org/10.1175/jcli3446.1>
1027
1028 Cook, K. H. (1999). Generation of the African easterly jet and its role in determining West
1029 African precipitation. *Journal of Climate*, 12(5), 1165– 1184.
1030 [https://doi.org/10.1175/1520-0442\(1999\)012<1165:gotaej>2.0.co;2](https://doi.org/10.1175/1520-0442(1999)012<1165:gotaej>2.0.co;2)
1031

1032 Cook, K. H., & Vizzy, E. K. (2006). Coupled model simulations of the West African monsoon
1033 system: Twentieth- and twenty-first-century simulations. *Journal of Climate*, 19(15), 3681–
1034 3703. <https://doi.org/10.1175/jcli3814.1>
1035

1036 Dee, D. P., Uppala, S. M., Simmons, A. J., Berrisford, P., Poli, P., Kobayashi, S., et al. (2011).
1037 The ERA-Interim reanalysis: Configuration and performance of the data assimilation system.
1038 *Quarterly Journal of the Royal Meteorological Society*, 137(656), 553–597.
1039 <https://doi.org/10.1002/qj.828>
1040

1041 Diallo, I., Bain, C. L., Gaye, A. T., Moufouma-Okia, W., Niang, C., Dieng, M. D. B., & Graham,
1042 R. (2014). Simulation of the West African monsoon onset using the HadGEM3-RA regional
1043 climate model. *Climate Dynamics*, 43(3–4), 575–594. [https://doi.org/10.1007/s00382-014-](https://doi.org/10.1007/s00382-014-2219-0)
1044 2219-0
1045

1046 Diallo, I., Giorgi, F., Deme, A., Tall, M., Mariotti, L., & Gaye, A. T. (2016). Projected changes of
1047 summer monsoon extremes and hydroclimatic regimes over West Africa for the twenty-first
1048 century. *Climate Dynamics*, 47(12), 3931–3954. <https://doi.org/10.1007/s00382-016-3052-4>
1049

1050 Diedhiou, A., Janicot, S., Viltard, A., de Felice, P., & Laurent, H. (1999). Easterly wave regimes
1051 and associated convection over West Africa and tropical Atlantic: Results from the
1052 NCEP/NCAR and ECMWF reanalyses. *Climate Dynamics*, 15(11), 795–822.
1053 <https://doi.org/10.1007/s003820050316>
1054

1055 Dixon, R. D., Daloz, A. S., Vimont, D. J., & Biasutti, M. (2017). Saharan heat low biases in
1056 CMIP5 models. *Journal of Climate*, 30(8), 2867–2884. [https://doi.org/10.1175/jcli-d-16-](https://doi.org/10.1175/jcli-d-16-0134.1)
1057 0134.1
1058

1059 Doblas-Reyes, F.J., A.A. Sörensson, M. Almazroui, A. Dosio, W.J. Gutowski, R. Haarsma, R.
1060 Hamdi, B. Hewitson, W.-T. Kwon, B.L. Lamptey, D. Maraun, T.S. Stephenson, I. Takayabu, L.
1061 Terray, A. Turner, and Z. Zuo, 2021: Linking Global to Regional Climate Change. In *Climate*
1062 *Change 2021: The Physical Science Basis. Contribution of Working Group I to the Sixth*
1063 *Assessment Report of the Intergovernmental Panel on Climate Change [Masson-Delmotte,*

1064 V., P. Zhai, A. Pirani, S.L. Connors, C. Péan, S. Berger, N. Caud, Y. Chen, L. Goldfarb, M.I.
1065 Gomis, M. Huang, K. Leitzell, E. Lonnoy, J.B.R. Matthews, T.K. Maycock, T. Waterfield, O.
1066 Yelekçi, R. Yu, and B. Zhou (eds.)). Cambridge University Press, Cambridge, United Kingdom
1067 and New York, NY, USA, pp. 1363–1512, doi:10.1017/9781009157896.012.
1068

1069 Dosio, A., Panitz, H.-J., Schubert-Frisius, M., & Lüthi, D. (2015). Dynamical downscaling of
1070 CMIP5 global circulation models over CORDEX-Africa with COSMO-CLM: Evaluation over the
1071 present climate and analysis of the added value. *Climate Dynamics*, 44(9–10), 2637–2661.
1072 <https://doi.org/10.1007/s00382-014-2262-x>
1073

1074 Dosio, A., Turner, A. G., Tamoffo, A. T., Sylla, M. B., Lennard, C., Jones, R. G., Hewitson, B.
1075 (2020). A tale of two futures: Contrasting scenarios of future precipitation for West Africa
1076 from an ensemble of regional climate models. *Environmental Research Letters*, 15(6),
1077 064007. <https://doi.org/10.1088/1748-9326/ab7fde>
1078

1079 Druyan, L. M., Feng, J., Cook, K. H., Xue, Y., Fulakeza, M., Hagos, S. M., ... Ibrah, S. S. (2009).
1080 The WAMME regional model intercomparison study. *Climate Dynamics*, 35(1), 175–
1081 192. <https://doi.org/10.1007/s00382-009-0676-7>
1082

1083 Engelstaedter, S., Washington, R., Flamant, C., Parker, D. J., Allen, C. J. T., & Todd, M. C.
1084 (2015). The Saharan heat low and moisture transport pathways in the central Sahara-
1085 Multi-aircraft observations and Africa-LAM evaluation. *Journal of Geophysical Research:*
1086 *Atmospheres*, 120(10), 4417–4442. <https://doi.org/10.1002/2015jd023123>
1087

1088 Eyring V, Bony S, Meehl GA, Senior CA, Stevens B, Stouffer RJ, Taylor KE (2016) Overview of
1089 the Coupled Model Intercomparison Project Phase 6 (CMIP6) experimental design and
1090 organization. *Geosci Model Dev* 9(5):1937–1958. <https://doi.org/10.5194/gmd-9-1937-2016>
1091

1092 Feser, F. (2006). Enhanced detectability of added value in limited-area model results
1093 separated into different spatial scales. *Monthly Weather Review*, 134(8), 2180–2190.
1094 <https://doi.org/10.1175/mwr3183.1>
1095

1096 Fontaine, B., Philippon, N., & Camberlin, P. (1999). An improvement of June September
1097 rainfall forecasting in the Sahel based upon region April-May moist static energy content
1098 (1968-1997). *Geophysical Research Letters*, 26(14), 2041–2044.
1099 <https://doi.org/10.1029/1999gl900495>
1100
1101 Funk, Chris, et al. “The Climate Hazards Infrared Precipitation with Stations—a New
1102 Environmental Record for Monitoring Extremes.” *Scientific Data*, vol. 2, no. 1, 2015,
1103 doi:10.1038/sdata.2015.66.
1104
1105 Gbode, I. E., Babalola, T. E., Diro, G. T., & Intsiful, J. D. (2023). Assessment of ERA5 and era-
1106 interim in reproducing mean and extreme climates over West Africa. *Advances in*
1107 *Atmospheric Sciences*, 40(4), 570–586. <https://doi.org/10.1007/s00376-022-2161-8>
1108
1109 Giannini, A. (2010). Mechanisms of climate change in the Semiarid African Sahel: The local
1110 view. *Journal of Climate*, 23(3), 743–756. <https://doi.org/10.1175/2009jcli3123.1>
1111
1112 Giannini, A., Salack, S., Lodoun, T., Ali, A., Gaye, A. T., & Ndiaye, O. (2013). A unifying view of
1113 climate change in the Sahel linking intra-seasonal, interannual and longer time scales.
1114 *Environmental Research Letters*, 8(2), 024010. [https://doi.org/10.1088/1748-](https://doi.org/10.1088/1748-9326/8/2/024010)
1115 [9326/8/2/024010](https://doi.org/10.1088/1748-9326/8/2/024010)
1116
1117 Gibba, P., Sylla, M. B., Okogbue, E. C., Gaye, A. T., Nikiema, M., & Kebe, I. (2018). State-of-
1118 the-art climate modeling of extreme precipitation over Africa: Analysis of CORDEX added-
1119 value over CMIP5. *Theoretical and Applied Climatology*, 137(12), 1041–1057.
1120 <https://doi.org/10.1007/s00704-018-2650-y>
1121
1122 Gutowski WJ et al (2016) WCRP coordinated regional downscaling experiment (CORDEX): a
1123 diagnostic MIP for CMIP6. *Geosci Model Dev* 9:4087–4095. [https://doi.org/10.5194/gmd-9-](https://doi.org/10.5194/gmd-9-4087-2016)
1124 [4087-2016](https://doi.org/10.5194/gmd-9-4087-2016)
1125
1126 Harris, I., Osborn, T. J., Jones, P., & Lister, D. (2020). Version 4 of the CRU TS monthly high-
1127 resolution gridded multivariate climate dataset. *Scientific Data*, 7(1), 109.

1128 <https://doi.org/10.1038/s41597-020-0453-3>
1129
1130 Hersbach H, Bell B, Berrisford P et al (2020) The ERA5 global reanalysis. Q J R Meteorol Soc.
1131 <https://doi.org/10.1002/qj.3803>
1132
1133 Hill, S. A., Ming, Y., Held, I. M., & Zhao, M. (2017). A moist static energy budget based
1134 analysis of the Sahel rainfall response to uniform oceanic warming. *Journal of Climate*,
1135 *30*(15), 5637–5660. <https://doi.org/10.1175/jcli-d-16-0785.1>
1136
1137 Hourdin, F., Musat, I., Guichard, F. se, Ruti, P. M., Favot, F., Filiberti, M.-A., Gallée, H. (2010).
1138 AMMA-Model intercomparison project. *Bulletin of the American Meteorological Society*,
1139 *91*(1), 95–104. <https://doi.org/10.1175/2009bams2791.1>
1140
1141 Hwang, Y., Frierson, D. M. W., & Kang, S. M. (2013). Anthropogenic sulfate aerosol and the
1142 southward shift of tropical precipitation in the late 20th century. *Geophysical Research*
1143 *Letters*, *40*(11), 2845–2850. <https://doi.org/10.1002/grl.50502>
1144
1145 Jacob, D., & Podzun, R. (1997). Sensitivity studies with the regional climate model REMO.
1146 *Meteorology and Atmospheric Physics*, *63*(1–2), 119–129.
1147 <https://doi.org/10.1007/bf01025368>
1148
1149 Jacob, D. (2001). The role of water vapour in the atmosphere. A short overview from a
1150 climate modeller’s point of view. *Physics and Chemistry of the Earth, Part A: Solid Earth and*
1151 *Geodesy*, *26*(6–8), 523–527. [https://doi.org/10.1016/s1464-1895\(01\)00094-1](https://doi.org/10.1016/s1464-1895(01)00094-1)
1152
1153 Jacob, D., Elizalde, A., Haensler, A., Hagemann, S., Kumar, P., Podzun, R., ... Wilhelm, C.
1154 (2012). Assessing the transferability of the regional climate model REMO to different
1155 coordinated regional climate downscaling experiment (CORDEX) regions. *Atmosphere*, *3*(1),
1156 181–199. <https://doi.org/10.3390/atmos3010181>
1157
1158 Janicot, S., Moron, V., & Fontaine, B. (1996). Sahel droughts and Enso dynamics. *Geophysical*
1159 *Research Letters*, *23*(5), 515–518. <https://doi.org/10.1029/96gl00246>

1160

1161 Jungclaus, J. H., Fischer, N., Haak, H., Lohmann, K., Marotzke, J., Matei, D., ...Storch, J. S.
1162 (2013). Characteristics of the ocean simulations in the Max Planck Institute Ocean Model
1163 (MPIOM) the ocean component of the MPI-Earth system model. *Journal of Advances in*
1164 *Modeling Earth Systems*, 5(2), 422–446. <https://doi.org/10.1002/jame.20023>

1165

1166 Kiladis, G. N., Thorncroft, C. D., & Hall, N. M. J. (2006). Three-Dimensional structure and
1167 dynamics of African easterly waves. Part I: Observations. *Journal of the Atmospheric*
1168 *Sciences*, 63(9), 2212–2230. <https://doi.org/10.1175/jas3741.1>

1169

1170 Koteswaram, P. (1958). The easterly jet stream in the Tropics. *Tellus*, 10(1), 43–57.
1171 <https://doi.org/10.1111/j.2153-3490.1958.tb01984.x>

1172

1173 Laprise, R., Hernández-Díaz, L., Tete, K., Sushama, L., Šeparović, L., Martynov, A.,... Valin, M.
1174 (2013). Climate projections over CORDEX Africa domain using the fifth-generation Canadian
1175 Regional Climate Model (CRCM5). *Climate Dynamics*, 41(11–12), 3219–3246.
1176 <https://doi.org/10.1007/s00382-012-1651-2>

1177

1178 Lavaysse, C., Flamant, C., Janicot, S., Parker, D. J., Lafore, J.-P., Sultan, B., & Pelon, J. (2009).
1179 Seasonal evolution of the West African heat low: A climatological perspective. *Climate*
1180 *Dynamics*, 33(2–3), 313–330. <https://doi.org/10.1007/s00382-009-0553-4>

1181

1182 Lavaysse, C., Flamant, C., & Janicot, S. (2010). Regional-scale convection patterns during
1183 strong and weak phases of the Saharan heat low. *Atmospheric Science Letters*, 11(4), 255–
1184 264. <https://doi.org/10.1002/asl.284>

1185

1186 Lavaysse, C., Chaboureau, J.-P., & Flamant, C. (2011). Dust impact on the West African heat
1187 low in summertime. *Quarterly Journal of the Royal Meteorological Society*, 137(658), 1227–
1188 1240. <https://doi.org/10.1002/qj.844>

1189

1190 Lavaysse, C. (2015). Saharan desert warming. *Nature Climate Change*, 5(9), 807–808.
1191 <https://doi.org/10.1038/nclimate2773>

1192

1193 Lemburg, A., Bader, J., & Claussen, M. (2019). Sahel rainfall–tropical easterly jet relationship
1194 on synoptic to intraseasonal time scales. *Monthly Weather Review*, 147(5), 1733–
1195 1752. <https://doi.org/10.1175/mwr-d-18-0254.1>

1196

1197 Leroux, S., & Hall, N. M. J. (2009). On the relationship between African easterly waves and
1198 the African easterly jet. *Journal of the Atmospheric Sciences*, 66(8), 2303–2316.
1199 <https://doi.org/10.1175/2009jas2988.1>

1200

1201 Martin ER, Thorncroft CD (2013) The impact of the AMO on the west African monsoon
1202 annual cycle. *Q J R Meteorol Soc* 140(678):31–46. <https://doi.org/10.1002/qj.2107>

1203

1204 Meehl, G. A., Covey, C., Delworth, T., Latif, M., McAvaney, B., Mitchell, J. F. B., ...Taylor, K. E.
1205 (2007). THE WCRP CMIP3 multimodel dataset: A new era in climate change research. *Bulletin*
1206 *of the American Meteorological Society*, 88(9), 1383–1394.
1207 <https://doi.org/10.1175/bams-88-9-1383>

1208

1209 Monerie, P.-A., Roucou, P., & Fontaine, B. (2013). Mid-century effects of Climate Change on
1210 African monsoon dynamics using the A1B emission scenario. *International Journal of*
1211 *Climatology*, 33(4), 881–896. <https://doi.org/10.1002/joc.3476>

1212

1213 Monerie, P.-A., Wainwright, C. M., Sidibe, M., & Akinsanola, A. A. (2020). Model
1214 uncertainties in climate change impacts on Sahel precipitation in ensembles of CMIP5 and
1215 CMIP6 simulations. *Climate Dynamics*, 55(5–6), 1385–1401.
1216 <https://doi.org/10.1007/s00382-020-05332-0>

1217

1218 Monerie, P.-A., Wilcox, L. J., & Turner, A. G. (2022). Effects of anthropogenic aerosol and
1219 greenhouse gas emissions on Northern Hemisphere monsoon precipitation:
1220 Mechanisms and uncertainty. *Journal of Climate*, 35(8), 2305–2326.
1221 <https://doi.org/10.1175/jcli-d-21-0412.1>

1222

1223 NASA (2016). Modern-Era Retrospective analysis for Research and Applications, version 2.
1224 Goddard Earth Sciences Data and Information Services Center, accessed 12 September 2017.
1225 <https://disc.gsfc.nasa.gov/daac-bin/FTPSubset.pl>
1226
1227 Nesbitt, S. W., Cifelli, R., & Rutledge, S. A. (2006). Storm morphology and rainfall
1228 characteristics of TRMM precipitation features. *Monthly Weather Review*, 134(10), 2702–
1229 2721. <https://doi.org/10.1175/mwr3200.1>
1230
1231 Niang, I., and Coauthors, 2014: Africa. Climate Change 2014: Impacts, Adaptation, and
1232 Vulnerability. Part B: Regional Aspects. Cambridge University Press, 1199–1265,
1233 https://www.ipcc.ch/site/assets/uploads/2018/02/WGIIAR5PartB_FINAL.pdf
1234
1235 Nicholson, S. E., & Grist, J. P. (2003). The seasonal evolution of the atmospheric circulation
1236 over West Africa and Equatorial Africa. *Journal of Climate*, 16(7), 1013–1030.
1237 [https://doi.org/10.1175/1520-0442\(2003\)016<1013:tseota>2.0.co;2](https://doi.org/10.1175/1520-0442(2003)016<1013:tseota>2.0.co;2)
1238
1239 Nicholson, Sharon E. (2013). The West African Sahel: A review of recent studies on the
1240 rainfall regime and its interannual variability. *ISRN Meteorology*, 2013, 1–32.
1241 <https://doi.org/10.1155/2013/453521>
1242
1243 Nicholson, S. E., Klotter, D., Zhou, L., & Hua, W. (2019). Validation of satellite precipitation
1244 estimates over the Congo Basin. *Journal of Hydrometeorology*, 20(4), 631–656.
1245 <https://doi.org/10.1175/jhm-d-18-0118.1>
1246
1247 Nicholson, Sharon E., & Klotter, D. (2020). The Tropical Easterly Jet over Africa, its
1248 representation in six reanalysis products, and its association with Sahel rainfall. *International*
1249 *Journal of Climatology*, 41(1), 328–347. <https://doi.org/10.1002/joc.6623>
1250
1251 d’Orgeval T. 2008. Impact du changement climatique sur la saison des pluies en Afrique de
1252 l’Ouest : que nous disent les modèles de climat actuels? *Science et changements planétaires*
1253 / *Sécheresse* 19(2): 79–85.
1254

1255 Paeth, H., Born, K., Podzun, R., & Jacob, D. (2005). Regional dynamical downscaling over
1256 West Africa: Model evaluation and comparison of wet and dry years. *Meteorologische*
1257 *Zeitschrift*, 14(3), 349–367. <https://doi.org/10.1127/0941-2948/2005/0038>
1258

1259 Paeth, H., & Mannig, B. (2012). On the added value of regional climate modeling in climate
1260 change assessment. *Climate Dynamics*, 41(3–4), 1057–1066.
1261 <https://doi.org/10.1007/s00382-012-1517-7>
1262

1263 Panitz, H.-J., Dosio, A., Büchner, M., Lüthi, D., & Keuler, K. (2014). COSMO-CLM (CCLM)
1264 climate simulations over CORDEX-Africa domain: Analysis of the ERA-Interim driven
1265 simulations at 0.44° and 0.22° resolution. *Climate Dynamics*, 42(11–12), 3015–3038.
1266 <https://doi.org/10.1007/s00382-013-1834-5>
1267

1268 Parker, D. J., Burton, R. R., Diongue-Niang, A., Ellis, R. J., Felton, M., Taylor, C. M.,...
1269 Tompkins, A. M. (2005). The diurnal cycle of the West African monsoon circulation.
1270 *Quarterly Journal of the Royal Meteorological Society*, 131(611), 2839–2860.
1271 <https://doi.org/10.1256/qj.04.52>
1272

1273 Patricola, C. M., & Cook, K. H. (2007). Dynamics of the West African monsoon under mid-
1274 holocene precessional forcing: Regional climate model simulations. *Journal of Climate*, 20(4),
1275 694–716. <https://doi.org/10.1175/jcli4013.1>
1276

1277 Paxian, A., Sein, D., Panitz, H.-J., Warscher, M., Breil, M., Engel, T., ... Paeth, H (2016). Bias
1278 reduction in decadal predictions of West African monsoon rainfall using regional climate
1279 models. *Journal of Geophysical Research: Atmospheres*, 121(4), 1715–1735.
1280 <https://doi.org/10.1002/2015jd024143>
1281

1282 Pu, B., & Cook, K. H. (2012). Role of the West African westerly jet in Sahel rainfall variations.
1283 *Journal of Climate*, 25(8), 2880–2896. <https://doi.org/10.1175/jcli-d-11-00394.1>
1284

1285 Pu, B., & Cook, K. H. (2010). Dynamics of the West African westerly jet. *Journal of Climate*,
1286 23(23), 6263–6276. <https://doi.org/10.1175/2010jcli3648.1>

1287

1288 Quagraine, K. A., Nkrumah, F., Klein, C., Klutse, N. A. B., & Quagraine, K. T. (2020). West
1289 african summer monsoon precipitation variability as represented by reanalysis datasets.
1290 *Climate*, 8(10), 111. <https://doi.org/10.3390/cli8100111>

1291

1292 Ratnam, J. V., Morioka, Y., Behera, S. K., & Yamagata, T. (2015). A model study of regional
1293 air-sea interaction in the austral summer precipitation over southern Africa. *Journal of*
1294 *Geophysical Research: Atmospheres*, 120(6), 2342–2357.
1295 <https://doi.org/10.1002/2014jd022154>

1296

1297 Redelsperger, J.-L., C. D. Thorncroft, A. Diedhiou, T. Lebel, D. J. Parker, and J. Polcher (2006),
1298 African Monsoon multidisciplinary analysis: An international research project and field
1299 campaign, *Bull. Am. Meteorol. Soc.*, 87(12), 1739–1746, doi:10.1175/BAMS-87-12-1739.

1300

1301 Rodríguez-Fonseca, B., Mohino, E., Mechoso, C. R., Caminade, C., Biasutti, M., Gaetani, M., ...
1302 Voldoire, A. (2015). Variability and predictability of West African droughts: A review on the
1303 role of sea surface temperature anomalies. *Journal of Climate*, 28(10), 4034–4060.
1304 <https://doi.org/10.1175/jcli-d-14-00130.1>

1305

1306 Saini, R., Wang, G., Yu, M., & Kim, J. (2015). Comparison of RCM and GCM projections of
1307 boreal summer precipitation over Africa. *Journal of Geophysical Research: Atmospheres*,
1308 120(9), 3679–3699. <https://doi.org/10.1002/2014jd022599>

1309

1310 Samanta, D., Hameed, S. N., Jin, D., Thilakan, V., Ganai, M., Rao, S. A., & Deshpande, M.
1311 (2018). Impact of a narrow Coastal Bay of Bengal Sea surface temperature front on an indian
1312 summer monsoon simulation. *Scientific Reports*, 8(1). [https://doi.org/10.1038/s41598-018-](https://doi.org/10.1038/s41598-018-35735-3)
1313 35735-3

1314

1315 Schepanski, K., Heinold, B., & Tegen, I. (2017). Harmattan, Saharan heat low, and West
1316 African monsoon circulation: Modulations on the Saharan dust outflow towards the North
1317 Atlantic. *Atmospheric Chemistry and Physics*, 17(17), 10223–10243.

1318 <https://doi.org/10.5194/acp-17-10223-2017>
1319
1320 Sein, D. V., Koldunov, N. V., Pinto, J. G., & Cabos, W. (2014). Sensitivity of simulated regional
1321 Arctic climate to the choice of coupled model domain. *Tellus A: Dynamic Meteorology and*
1322 *Oceanography*, 66(1), 23966. <https://doi.org/10.3402/tellusa.v66.23966>
1323
1324 Sein, D. V., Mikolajewicz, U., Gröger, M., Fast, I., Cabos, W., Pinto, J. G., ... Jacob, D. (2015).
1325 Regionally coupled atmosphere-ocean-sea ice-marine biogeochemistry model ROM: 1.
1326 Description and validation. *Journal of Advances in Modeling Earth Systems*, 7(1), 268–
1327 304. <https://doi.org/10.1002/2014ms000357>
1328
1329 Schneider, Udo; Hänsel, Stephanie; Finger, Peter; Rustemeier, Elke; Ziese, Markus (2022):
1330 GPCP Full Data Monthly Product Version 2022 at 0.25°: Monthly Land-Surface
1331 Precipitation from Rain-Gauges built on GTS-based and Historical Data. DOI:
1332 10.5676/DWD_GPCC/FD_M_V2022_025
1333
1334 Song, F., Leung, L. R., Lu, J., & Dong, L. (2018). Seasonally dependent responses of
1335 subtropical highs and tropical rainfall to anthropogenic warming. *Nature Climate Change*,
1336 8(9), 787–792. <https://doi.org/10.1038/s41558-018-0244-4>
1337
1338 Stevens, B., Giorgetta, M., Esch, M., Mauritsen, T., Crueger, T., Rast, S., Roeckner, E. (2013).
1339 Atmospheric component of the MPI-M Earth System Model: ECHAM6. *Journal of Advances*
1340 *in Modeling Earth Systems*, 5(2), 146–172. <https://doi.org/10.1002/jame.20015>
1341
1342 Sultan, B., & Janicot, S. (2003). The West African monsoon dynamics. Part II: The “Preonset”
1343 and “onset” of the Summer Monsoon. *Journal of Climate*, 16(21), 3407–3427.
1344 [https://doi.org/10.1175/1520-0442\(2003\)016<3407:twamdp>2.0.co;2](https://doi.org/10.1175/1520-0442(2003)016<3407:twamdp>2.0.co;2)
1345
1346 Tamoffo, A. T., Dosio, A., Vondou, D. A., & Sonkoué, D. (2020). Process-Based analysis of the
1347 added value of dynamical downscaling over central africa. *Geophysical Research Letters*,
1348 47(17). <https://doi.org/10.1029/2020gl089702>
1349

1350 Tamoffo, A. T., Dosio, A., Amekudzi, L. K., & Weber, T. (2022). Process-oriented evaluation of
1351 the West African Monsoon system in CORDEX-CORE regional climate models. *Climate*
1352 *Dynamics*, 60(9–10), 3187–3210. <https://doi.org/10.1007/s00382-022-06502-y>
1353

1354 Tamoffo, A. T., Akinsanola, A. A., & Weber, T. (2023). Understanding the diversity of the
1355 West African monsoon system change projected by CORDEX-CORE regional climate models.
1356 *Climate Dynamics*. <https://doi.org/10.1007/s00382-023-06690-1>
1357

1358 Tamoffo, A. T., Weber, T., Cabos, W., Sein, D. V., Dosio, A., Rechid, D., ... Jacob, D. (2024).
1359 Mechanisms of added value of a coupled global ocean-regional atmosphere climate model
1360 over Central Equatorial Africa. *Journal of Geophysical Research: Atmospheres*, 129(3).
1361 <https://doi.org/10.1029/2023jd039385>
1362

1363 Taylor KE, Stouffer RJ, Meehl GA (2012) An overview of CMIP5 and the experiment design.
1364 *Bull Am Meteorol Soc* 93:485–498. <https://doi.org/10.1175/BAMS-D-11-00094.1>
1365

1366 Thorncroft, C. D., & Blackburn, M. (1999). Maintenance of the African easterly jet. *Quarterly*
1367 *Journal of the Royal Meteorological Society*, 125(555), 763–786.
1368 <https://doi.org/10.1002/qj.49712555502>
1369

1370 Thorncroft, C. D., Parker, D. J., Burton, R. R., Diop, M., Ayers, J. H., Barjat, H., Tompkins, A. M.
1371 (2003). The JET2000 project: Aircraft observations of the African easterly jet and African
1372 easterly waves. *Bulletin of the American Meteorological Society*, 84(3), 337–352.
1373 <https://doi.org/10.1175/bams-84-3-337>
1374

1375 Thorncroft, C. D., Hall, N. M. J., & Kiladis, G. N. (2008). Three-Dimensional structure and
1376 dynamics of African easterly waves. Part III: Genesis. *Journal of the Atmospheric Sciences*,
1377 65(11), 3596–3607. <https://doi.org/10.1175/2008jas2575.1>
1378

1379 Vizy, E. K., and K.H. Cook, (2002). Development and application of a mesoscale climate
1380 model for the tropics: Influence of sea surface temperature anomalies on the West African
1381 monsoon. *Journal of Geophysical Research*, 107(D3). <https://doi.org/10.1029/2001jd000686>
1382

1383 Vizy, E. K., & Cook, K. H. (2009). A mechanism for African monsoon breaks: Mediterranean
1384 cold air surges. *Journal of Geophysical Research: Atmospheres*, 114(D1).
1385 <https://doi.org/10.1029/2008jd010654>
1386

1387 Vizy, E. K., Cook, K. H., Crétat, J., & Neupane, N. (2013). Projections of a wetter Sahel in
1388 the twenty-first century from global and regional models. *Journal of Climate*, 26(13), 4664–
1389 4687. <https://doi.org/10.1175/jcli-d-12-00533.1>
1390

1391 Weber, Torsten, Cabos, W., Sein, D. V., & Jacob, D. (2022). Benefits of simulating
1392 precipitation characteristics over Africa with a regionally-coupled atmosphere ocean model.
1393 *Climate Dynamics*, 60(3–4), 1079–1102. <https://doi.org/10.1007/s00382-022-06329-7>
1394

1395 Whittleston, D., Nicholson, S. E., Schlosser, A., & Entekhabi, D. (2017). Climate models lack
1396 jet–rainfall coupling over West Africa. *Journal of Climate*, 30(12), 4625–4632.
1397 <https://doi.org/10.1175/jcli-d-16-0579.1>
1398

1399 Wu, M., Nikulin, G., Kjellström, E., Belušić, D., Jones, C., & Lindstedt, D. (2020). The impact of
1400 regional climate model formulation and resolution on simulated precipitation in Africa. *Earth*
1401 *System Dynamics*, 11(2), 377–394, <https://doi.org/10.5194/esd-11-377-2020>
1402

1403 Xue, Y., De Sales, F., Lau, W. K.-M., Boone, A., Feng, J., Dirmeyer, P., ... Wu, M.-L. C. (2010).
1404 Intercomparison and analyses of the climatology of the West African Monsoon in the West
1405 African Monsoon Modeling and Evaluation project (WAMME) first model intercomparison
1406 experiment. *Climate Dynamics*, 35(1), 3-27. <https://doi.org/10.1007/s00382-010-0778-2>
1407

1408 Zhao, Y., Braconnot, P., Marti, O., Harrison, S. P., Hewitt, C., Kitoh, A., ... Weber, S. L. (2005).
1409 A multi-model analysis of the role of the ocean on the African and Indian monsoon during
1410 the mid-Holocene. *Climate Dynamics*, 25(7–8), 777–800.

1411 <https://doi.org/10.1007/s00382-005-0075-7>
1412
1413 Zhou T, Lu J, Zhang W, Chen Z (2020) The sources of uncertainty in the projection of global
1414 land monsoon precipitation. *Geophys Res Lett.* <https://doi.org/10.1029/2020gl088415>
1415
1416 Zhu, S., Remedio, A. R. C., Sein, D. V., Sielmann, F., Ge, F., Xu, J., ... Zhi, X. (2020). Added
1417 value of the regionally coupled model ROM in the East Asian summer monsoon modeling.
1418 *Theoretical and Applied Climatology*, 140(1–2), 375–387. [https://doi.org/10.1007/s00704-](https://doi.org/10.1007/s00704-020-03093-8)
1419 [020-03093-8](https://doi.org/10.1007/s00704-020-03093-8)
1420
1421 Zou, L., & Zhou, T. (2016). A regional ocean–atmosphere coupled model developed for
1422 CORDEX East Asia: Assessment of Asian summer monsoon simulation. *Climate Dynamics*,
1423 47(12), 3627–3640. <https://doi.org/10.1007/s00382-016-3032-8>
1424
1425
1426
1427
1428
1429
1430
1431
1432
1433
1434
1435
1436